Politecnico di Torino

Master Degree in Quantum Engineering

Experimental Realization of a Compact Warm-Vapor Rubidium Atomic Clock

Candidate:

Federico Muscarà

******

Supervisors:

Prof. Roberto Proietti

Dott. Ric. Massimiliano Proietti

Dott. Ric. Marco Menchetti

Politecnico di Torino

March 2026

Abstract

Optical atomic clocks represent the state of the art in timekeeping, playing a key role in the scientific community and technological applications. Today, the most accurate optical clocks are based on ultracold atoms or ions, but their complexity and size limit their use outside of laboratory environments. In this context, the development of compact optical frequency standards based on warm atomic vapors has attracted increasing attention, with the potential to enable a wide range of applications in fundamental science, aerospace, and industry.

This thesis, conducted in collaboration with the quantum sensing group at Leonardo Quantum Laboratories, presents the realization of an initial design of a warm-vapor rubidium atomic clock based on the two-photon transition driven at 778 nm. This approach allows for Doppler-free high-SNR readout by detecting atomic fluorescence at 420 nm, enabling the observation of the two-photon spectrum of both ^{87}Rb and ^{85}Rb. These results allow laser locking to the $5S_{1/2} \rightarrow 5D_{5/2}$ transition of ^{87}Rb, leading to an estimated detection-noise-limited short-term stability of $\sigma_y(\tau) \approx 3.67 \times 10^{-13}/\sqrt{\tau}$.

The 778 nm wavelength can be conveniently generated through Second Harmonic Generation with a non linear crystal, integrating mature C-band laser sources at 1556 nm. For this reason, this work includes the design of an optical cavity to enhance the SHG conversion efficiency, with simulations predicting more than 0.5 W of output power at 778 nm starting from 2 W at 1556 nm.

Contents

List of Figures

List of Tables

Chapter 1

Introduction

1.1 Background and motivation

High-precision timekeeping is a cornerstone of both fundamental science and technological innovation, with atomic frequency standards providing accurate, stable devices that enable frequency and time measurement with extraordinary precision.

Within the metrological community, atomic clocks have been essential for defining the second, which is now being redefined through the transition to optical frequency standards [1]. In the realm of scientific research, they have fundamental importance in several applications. For instance, they enable Very Long Baseline Interferometry (VLBI) by synchronizing telescopes across the globe [2], while they support the monitoring of geophysical phenomena in seismology [3]. Searching for temporal variations in fundamental constants and verifying general relativity through chronometric geodesy are other applications in fundamental physics [4, 5].

Beyond the scientific community, high-accuracy timing has a strong impact on the aerospace and industrial sectors [6]. Qualified atomic clocks are integrated into deep-space missions [7] or serve as synchronization devices for global navigation systems [8]. Finally, telecommunications and timestamping [9] of financial transactions all rely on stable and accurate frequency references and timekeeping enabled by atomic frequency standards and clocks.

In this broad and demanding context, research on next-generation atomic clocks has accelerated worldwide, with increasing attention toward quantum technologies.

This thesis project is inserted within this framework, as part of the activities carried out at Leonardo Quantum Labs in the field of quantum sensing and atomic clocks. The work presented here specifically concerns the realization of an atomic clock based on warm rubidium vapor. The approach exploits the two-photon transition of rubidium using second-harmonic-generated light at 778*nm*, with detection of the associated 420*nm* fluorescence, offering a promising path toward compact and robust quantum frequency standards.

1.2 Thesis Outline

The following provides a brief overview of the thesis structure and the main topics addressed in each chapter.

Chapter 2 introduces the fundamental principles of atomic frequency standards with a focus on rubidium-based devices. It reviews fine and hyperfine structure in rubidium and highlights Doppler-free spectroscopy techniques as the basis for the two-photon transition studied in this work.

Chapter 3 presents the theoretical background of nonlinear optics, with a particular emphasis on second harmonic generation and suitable nonlinear crystals for frequency doubling.

Chapter 4 discusses the theory of the confocal resonator, before describing the design and the expected performance of the second harmonic generation enhancement cavity that will be used to generate the 778*nm* light for the rubidium two-photon transition.

Chapter 5 describes the complete experimental setup developed for the realization of the rubidium two-photon atomic clock, presenting spectroscopy results and clock performance.

Chapter 6 explores potential developments for the clock stability characterization and future improvements of the experimental setup.

Finally, Chapter 7 summarizes the key findings of the thesis, reflecting on the implications of the work.

Chapter 2

Atomic Frequency Standards

2.1 Introduction

Quantum sensors are devices that use quantum effects to deliver high accuracy and long-term stability. Atomic clocks and magnetometers, for example, use energy-level quantization to suppress drift (a systematic, time-dependent frequency change) and aging effects common in classical references. In contrast, cheap quartz oscillators rely on mechanical vibrations in a large crystal that physically ages and changes structure, causing frequency drift over weeks or months.

2.1.1 AFS Preliminaries

An atomic frequency standard (AFS) is a device that locks a macroscopic local oscillator (LO) (a quartz oscillator in the microwave range or a laser in the optical domain) to a well-defined atomic transition [10]. Its strenght comes from two features: identical atoms provide reproducible references under fixed conditions[1] and an unperturbed transition frequency is, in principle, constant in time[2]. In metrological terminology, a standard is considered "primary" when it directly realizes the SI unit definition without requiring calibration against another reference. Currently, caesium-133 clocks are primary standards for the second, as the SI definition is based on

[1] According to Standard Model and Relativity.

[2] If fundamental constants of nature are stable in time. String Theory postulates the variation of constants in time, but it has not been proved yet.

the caesium hyperfine transition (Section 2.2.4). Other atomic clocks, including optical standards with superior accuracy, are classified as secondary standards until a potential redefinition of the second.

Operationally, focusing on the optical domain, an AFS consists of a laser whose frequency is locked to an atomic transition via a feedback control loop that keeps the laser centered on the atomic resonance. However, not all atomic transitions are suitable for frequency standards. A good clock transition should link long-lived states to enable extended interrogation times and it should exhibit a narrow natural linewidth to allow precise frequency determination (equation 2.6). It should also be less sensitive to external perturbations such as magnetic fields, electric fields, and collisional shifts. Additionally, it would be preferable if the transition is accessible with available laser technology and provides sufficient signal strength for efficient detection. By preparing the reference atomic system in such a stable state with no radiative decay, the local oscillator is then capable of offering a precise and tunable nominal frequency ν. Once established, the interaction between the atoms and the electromagnetic field can be expressed based on Planck's quantum relation, which states that the energy difference between two atomic states is related to the photon's frequency ν by:

$$E = h\nu \tag{2.1}$$

If the atomic transition frequency is matched, the atoms in the ensemble will experience a transition from the initial stable state to a final energetic state.

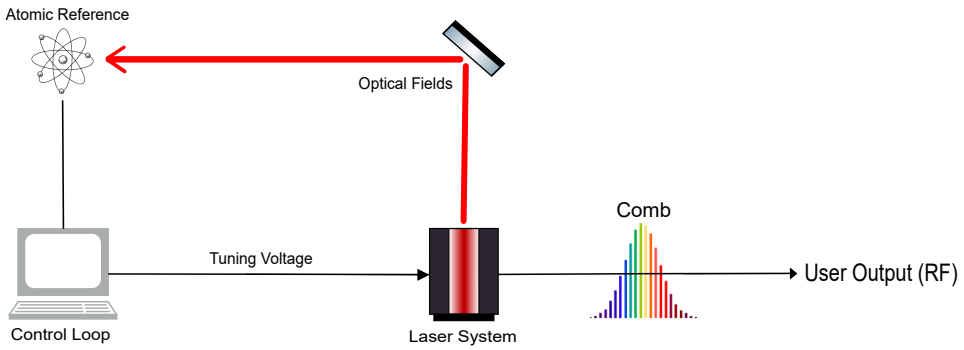

Fig. 2.1 Schematic representation of an atomic frequency standard.

A measurement stage allows for "counting" the number of atoms that have undergone the transition. Depending on the number of transitions, the frequency of the local oscillator is corrected with the aim of maximizing the excited population using a closed feedback loop (Figure 2.1). In practice, the laser frequency is adjusted to maximize a suitable spectroscopic signal, so that the laser is locked to the atomic resonance with high accuracy (see Chapter 5). Finally, the laser output signal can be used as a frequency reference once converted from the optical domain to the RF domain. The conversion is required because most practical applications (telecommunications, navigation systems, and general electronic instrumentation) operate in the RF region, rather than at optical frequencies.

Such conversion was not trivial until the advent of optical frequency combs in the early 2000s [11], which allowed to avoid complicated harmonic chains. A frequency comb is generated by a mode-locked pulsed laser (typically a femtosecond laser) that produces a spectrum consisting of a series of discrete, equidistant frequency lines. The comb acts as a "ruler" in the frequency domain, providing a direct link between optical frequencies ($\sim 10^{15}$ Hz) and measurable radio frequencies. Its spectrum can be described by the repetition rate f_{rep} (the spacing between adjacent lines, typically in the range of tens to hundreds of MHz) and the carrier-envelope offset frequency f_{ceo} (typically a few MHz):

$$\nu_n = n f_{\text{rep}} + f_{\text{ceo}} \tag{2.2}$$

where n is a large integer representing the mode number. Both f_{rep} and f_{ceo} can be stabilized to RF references and directly measured with electronic counters. In the context of atomic frequency standards, where the laser frequency is known from spectroscopy, the comb directly detects the RF beat note between the clock laser and the nearest comb mode ν_n. This beat frequency, typically in the MHz range and measurable with standard frequency counters, establishes the previously missing link connecting the optical frequency of the clock laser to the radio frequency domain.

2.1.2 AFS Performance Estimators

An atomic clock is a continuously operating atomic frequency standard. Its first practical realization was based on the hyperfine transitions of caesium atoms [12], which still defines the second in the International System of Units (SI) [1].

Current atomic clocks generate an RF output signal. If we call it f_0, the dimensionless quantity that describes the relative deviation of the clock frequency $f(t)$ from its nominal frequency is given by:

$$y(t) = \frac{f(t) - f_0}{f_0} \tag{2.3}$$

In this context, the performance of an atomic clock is commonly expressed in terms of two parameters: accuracy and instability. Clock accuracy quantifies how closely the measured frequency f_0 approximates the ideal unperturbed atomic transition frequency. It is fundamentally limited by systematic effects, which can be classified into environmental perturbations (such as magnetic and electric fields, temperature variations, and collisional shifts) and technical imperfections in the interrogation process (laser frequency offsets, intensity fluctuations).

On the other hand, clock instability is a statistical measure that quantifies the random fluctuations of the frequency output $f(t)$ around its nominal value f_0. Unlike systematic shifts, instability arises from stochastic processes such as thermal noise, quantum projection noise, and laser phase noise and it's commonly expressed in terms of the Allan deviation (ADEV) $\sigma_y(\tau)$ [13]. More in detail, $\sigma_y(\tau)$ describes the instability of the fractional frequency $y(t)$ over a certain averaging time τ. The corresponding variance (AVAR) is expressed as:

$$\sigma_y^2(\tau) = \frac{1}{2(M-1)} \sum_{m=0}^{M} (\bar{y}_{m+1} - \bar{y}_m)^2, \tag{2.4}$$

where $\bar{y}_m$ is the average fractional frequency over the m-th time interval of duration τ, and M is the total number of such intervals in the dataset.

On a logaritmic plot of $\sigma_y(\tau)$ versus τ, common clock noise processes appear as straight segments with characteristic slopes. Therefore, it is conventional to express the Allan variance as a sum of power-law terms:

$$\sigma_y^2(\tau) = \sum_{i=-2}^{+2} h_i \tau^i, \tag{2.5}$$

where the exponent i determines the slope and corresponds to a specific noise type. For example, from Figure 2.2 a first region of white noise is visible (τ^{-1}), followed by a flicker noise floor (τ^0) and a random walk region at longer timescales (τ^{+1}).

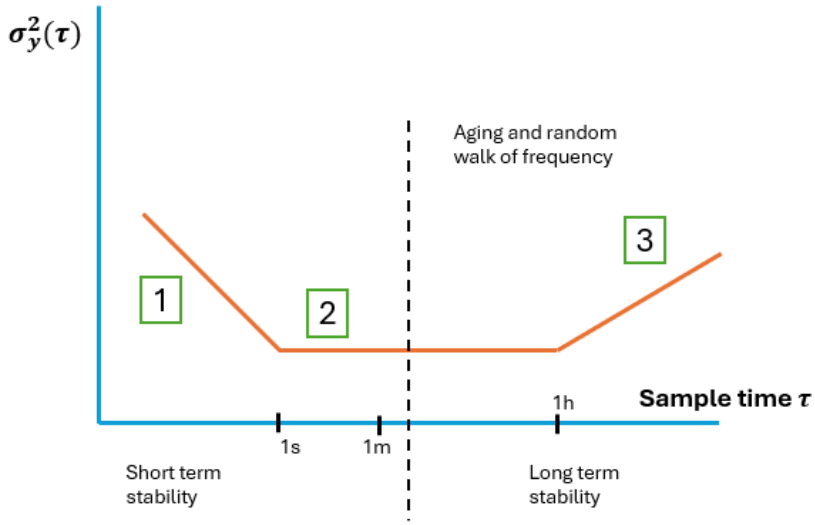

Fig. 2.2 Typical Allan variance plot showing different noise types.

In clock applications, we usually discuss short-term and long-term stability separately. For long-term stability, we're generally stuck with "colored" noise, such as flicker and random walk. Those come from electronics and other environmental factors, which we can only control to a certain extent. Short-term stability instead, is fundamentally determined by the atomic physics of our transition, such as quantum projection noise and the precision of quantum state preparation. The goal is to reach the white noise regime ($\tau^{-1/2}$ in ADEV) where these fundamental limits dominate. Mathematically, such limit to clock instability can be easily expressed as:

$$\sigma_y(\tau) \geq \frac{\Delta_\nu}{\nu_0} \frac{1}{SNR\sqrt{\tau}} = \frac{1}{Q} \frac{1}{SNR\sqrt{\tau}}, \tag{2.6}$$

where τ is the total interrogation time, Δ_ν is the transition linewidth and *SNR* is the signal-to-noise ratio of the atomic detection. So, equation 2.6 shows that instability improves (decreases) with increasing interrogation time τ and increases inversely with the transition quality factor $Q = \nu_0/\Delta_\nu$. This equation highlights the fundamental goals of atomic clock design: to achieve the narrowest possible transition linewidth Δ_ν by using long-lived states and longer interrogation times, while also maximizing the signal-to-noise ratio *SNR* of the atomic detection.

In this context, optical transitions have a significant advantage over microwave transitions, since optical frequencies are typically $\sim 10^{15}$ Hz compared to microwave frequencies around 10^{10} Hz in common standards. For similar transition linewidths, this results in quality factors approximately five orders of magnitude higher, resulting in much lower fundamental instability limits. However, working at optical frequencies brings significant technical challenges. Advanced laser systems with very stable frequencies are needed, often achieved by stabilizing lasers to optical cavities. Detecting and controlling optical transitions requires complex setups, such as frequency combs and advanced laser-cooling techniques, along with strict environmental controls to reduce systematic shifts. Despite these challenges, the improvements in instability and accuracy position optical frequency standards as the top choice for next-generation atomic clocks and for future redefinition of the SI second.

2.2 Rubidium Frequency Standard

2.2.1 Motivations

Atomic frequency standards can be broadly classified into laboratory-based primary standards, ground-based portable (and commercial) clocks and space-based standards, each optimized for specific performance metrics and application requirements [14].

Laboratory-based clocks, such as caesium fountains and optical lattice clocks, provide the highest levels of accuracy and stability. Caesium fountain clocks serve as primary frequency standards, achieving flicker noise fractional frequency uncertainties around 10^{-16} [15] and defining the SI second through caesium-133 hyperfine transitions. Optical clocks based on trapped ions (such as Al^+, Sr^+, Yb^+) or optical lattices (Sr, Yb) now demonstrate flicker noise instability below 10^{-18} [16, 17], representing the frontier of precision timekeeping and candidates for redefining

the second. However, these laboratory systems require substantial infrastructure, including vacuum chambers, laser cooling systems, and complex optical setups with volumes exceeding 1000 liters.

Portable and commercial standards prioritize reliability, size, and operational simplicity. Active hydrogen masers (AHMs) excel in medium-term stability (hours to days) with instabilities around 10^{-15} at flicker noise floor, though they typically weigh more than 200kg [18]. On the other hand, caesium beam tubes, typically mounted on racks, achieve stability around 10^{-13}, limited by shot noise in the beam current [19]. The caesium beam clocks and AHM clocks are now employed in National Metrological Institutes to maintain the precise world time.

Hydrogen masers have also been deployed in space applications, where passive hydrogen masers (PHMs) are used in GNSS constellations due to their superior long-term stability. However, PHMs are significantly bulkier and more expensive than alternative technologies. This trade-off reflects the empirical law stating that frequency stability generally improves as the size, mass, and power consumption of atomic clocks increase [20]. In applications where size, weight, and power (SWaP) constraints are critical, compact atomic clocks become essential.

Laboratory standards are simply impractical for these environments and it's precisely in this regime that rubidium frequency standards play their fundamental role, offering a favorable compromise between performance and portability.

2.2.2 Rubidium Standard Architectures

Rubidium frequency standards appeared in the late 1950s from optical pumping work at Princeton, leading to the first practical devices using microwave discharge lamps to optically pump and detect the ground state hyperfine transition near 6.8 GHz [21]. These rubidium clocks became popular because they offer a great balance of stability, size, weight, power, and cost compared to caesium beam clocks and hydrogen masers. Their use in GPS satellites helped prove Rb standards as reliable references, achieving medium-term frequency stabilities close to 10^{-14} over one day. While their long-term stability is limited by interactions with buffer gases and cell walls, Rb clocks meet current navigation needs thanks to their compact size and reliability, which outweigh the stability benefits of larger devices. For example, passive hydrogen masers used in ESA's Galileo navigation system provide better

long-term stability but have much higher size, weight, and power requirements: 28dm^3 volume (versus 3dm^3 for Rb), 18 kg mass (4 kg for Rb), and 80 W power consumption (18 W for Rb) [14].

Over the years, new developments have created a variety of rubidium standard designs, ranging from ultra-compact devices for portable use to high-performance systems for metrology research.

In terms of compactness, coherent population trapping (CPT) methods remove the microwave cavity completely, allowing chip-scale atomic clocks (CSACs) with volumes under 17 cm^3 [20]. These devices trade some stability (typically $\sim 10^{-10}$ at one day) to achieve exceptional miniaturization, making them ideal for portable military systems and underwater navigation.

Conversely, rubidium has also been developed into high-performance laboratory standards that focus on stability and accuracy rather than portability. Cold-atom rubidium fountain clocks, created in the 2000s and 2010s, use laser cooling and Ramsey interrogation to achieve fractional frequency instabilities around $2 \times 10^{-13}\tau^{-1/2}$ and long-term stability better than 10^{-15} [22], nearly matching the performance of caesium fountain clocks.

More recently, warm-vapor optical rubidium clocks based on the two-photon $5S \rightarrow 5D$ transition have gained renewed interest for their high quality factor and Doppler-free operation, linking traditional microwave standards and next-generation optical atomic clocks [23].

In this thesis, the broader motivations and recent results for optical operation on the rubidium two photon transition are deferred to the dedicated chapter presenting the clock implementation. In the next sections, the energy spectrum of multi-electron atoms is presented with analysis on fine and hyperfine structure of rubidium, together with a final emphasis on saturated absorption spectroscopy as the basis of the two photon transition interrogated in our clock.

2.2.3 Central Field Approximation

The simplest treatment of the energy levels of multi-electron atoms relies on the central field approximation (CFA) [24], which assumes that each electron moves in an average potential created by the nucleus and the other electrons. This allows us to

define single-electron quantum numbers n, l, s, m_l and m_s. The principal quantum number n characterizes the radial distribution of the electron wavefunction, while the azimuthal quantum number l defines its angular dependence (and the magnitude of the orbital angular momentum $\vec{l}$ of an individual electron). The quantum number n is an integer greater than zero, while accepted values for l range from 0 to $n-1$. The magnetic quantum number m_l specifies the orientation of the orbital angular momentum, expressing the projection of $\vec{l}$ on a chosen quantization axis, and its allowed values go from $-l$ to $+l$. The spin quantum number $s = 1/2$ represents the intrinsic angular momentum $\vec{s}$ of an individual electron and, finally, the spin magnetic quantum number m_s indicates the orientation of the electron's spin (allowed values $\pm 1/2$).

Rubidium (Rb) has atomic number $Z = 37$ and its electronic configuration in the ground state is $1s^2 2s^2 2p^6 3s^2 3p^6 4s^2 3d^{10} 4p^6 5s^1$, with filled shells to the $4p$ level and a single valence electron in the $5s$ orbital. The integers 1 through 5 represent the principal quantum number n, while the letters s, p, and d correspond to azimuthal quantum numbers $l = 0$, $l = 1$, and $l = 2$, respectively. Superscripts indicate the number of electrons in each subshell.

2.2.4 Fine and Hyperfine Energy Levels

Coulomb interaction between the pairs of electrons and between electrons and the nucleus causes deviations from the CFA potential. Additionally, the spin-orbit interaction, which couples the electron's spin and orbital angular momentum, is not taken into account in the CFA as well. These effects lead to the splitting of atomic energy levels into finer sub-levels, a phenomenon known as fine structure, better described in the Russel-Sounders "*L-S*" coupling scheme [25], where L is the magnitude of the total orbital angular momentum $\vec{L} = \sum_i \vec{l}_i$ and S is the magnitude of the total spin angular momentum $\vec{S} = \sum_i \vec{s}_i$ of a CFA atomic level. These two vectors couple to form the total angular momentum $\vec{J} = \vec{L} + \vec{S}$. The corresponding quantum number J can take values from $|L-S|$ to $L+S$ in integer steps. Each fine structure level corresponding to a CFA orbital configuration is labeled by the term ${}^{2S+1}L_J$, where the symbol $2S+1$ is the multiplicity of the level and L is represented by a letter, S, P and D for $L = 0, 1, 2$ respectively. Finally, the value of J is given as a subscript to L.

For the Rubidium $5s$ ground state configuration the only allowed values of L, S and J are defined by the only valence electron: $L = 0$, $S = 1/2$ and $J = 1/2$. On the other hand, in any filled orbital, L and S are both zero. Therefore, the ground state fine energy level for Rb is identified as $^2S_{1/2}$. The next Rb excited state is obtained by promoting the valence electron to the $5p$ orbital, with no change on the description of the remaining electrons. This configuration is described by $L = 1$, $S = 1/2$, which leads to two allowed values of J: $J = 1/2$ and $J = 3/2$. Consequently, the $5p$ excited state is split into two possible fine structure levels: $^2P_{1/2}$ and $^2P_{3/2}$.

Each fine structure level is further split into hyperfine levels due to the interaction between the nuclear spin I and the total electronic angular momentum J. Values of I depend on the nuclear structure and vary with the isotope. In any case, the nuclear magnetic moment proportional to I is much smaller than the electronic magnetic moment, so hyperfine splittings are typically several orders of magnitude smaller than fine structure splittings. Hyperfine levels are addressed with the total angular momentum F, given by the vector sum $F = I + J$. Its magnitude F can take values from $|I - J|$ to $I + J$ in integer steps, defining levels with slightly different energies.

Rubidium has two naturally occurring isotopes: ^{85}Rb and ^{87}Rb, with nuclear spins $I = 5/2$ and $I = 3/2$, respectively. Therefore, for the ground state $^2S_{1/2}$ ($J = 1/2$), ^{85}Rb has two hyperfine levels with $F = 2$ and $F = 3$ (Figure 2.3 [26]), while ^{87}Rb has $F = 1$ and $F = 2$ hyperfine levels. The energy difference between these two ground state hyperfine levels is 3.035 GHz for ^{85}Rb and 6.834 GHz for ^{87}Rb [27, 28].

2.2.5 Resolving Hyperfine Structure: Doppler-Free Spectroscopy

An atomic gas or vapor will absorb laser light close to a resonant transition linking its ground state to an excited state. As explained with equation 2.1, the atom will absorb a photon when the photon energy matches the energy gap between the two addressed levels, $|g\rangle$ and $|e\rangle$ (respectively ground and excited state).

Given a vapor cell filled with rubidium atoms interacting with a laser, the variation in beam intensity as it propagates through the medium can be described by the Lambert-Beer law:

$$I(\omega_L, L) = I(\omega_L, 0)e^{-\kappa(\omega_L)L} \tag{2.7}$$

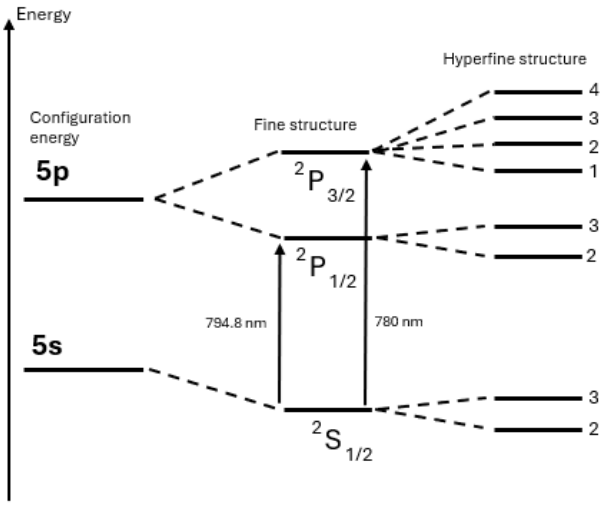

Fig. 2.3 ^{85}Rb lowest energy levels including fine and hyperfine structure (not in scale).

The equation represents an exponential decay of the intensity of the laser as it propagates through the vapor, where the absorption coefficient κ determines the rate of extinction. The absorption coefficient, in absence of line broadening mechanisms is theoretically estimated as [29]:

$$\kappa(\omega_L) = \frac{g_e}{g_g} \cdot \frac{\pi \omega_{ge} d_{ge}^2 n}{\varepsilon_0 \bar{h} c} \cdot g(\omega_L, \omega_{ge}) \tag{2.8}$$

where ω_{ge} is the atomic transition frequency, d_{ge} is the transition dipole moment, g_g and g_e are the degeneracy of the ground and excited state. The factor g is a line shape function, which arises due to the finite lifetime of the excited state.

In a thermal vapor, atomic motion introduces a Doppler shift so that the atoms experience a different laser frequency:

$$\omega_L' = \omega_L - \vec{k} \cdot \vec{v} \tag{2.9}$$

where $\vec{k}$ is the laser wavevector, $\vec{v}$ is the velocity of the atom with respect to the laboratory frame. If the atom is at rest ($v = 0$), the observed laser frequency remains unchanged ($\omega_L' = \omega_L$). However, for moving atoms ($v \neq 0$) the perceived frequency shifts, appearing either higher or lower than the nominal laser frequency

ω_L, depending on the direction of motion. Therefore, since each absorber can have a different velocity, they will be resonant and absorb at a different frequency: this Doppler shift contributes to broadening the absorption profile in atomic spectroscopy (Figure 2.4).

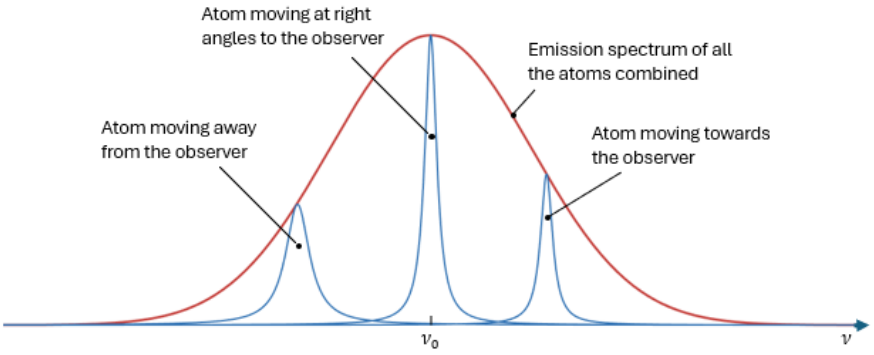

Fig. 2.4 Example of doppler-broadened absorption profile

Since the experiment involves a gas, the atoms exhibit a velocity distribution described by the Maxwell Boltzmann distribution:

$$f(v)dv = \sqrt{\frac{M}{2\pi k_B T}} \exp\left(-\frac{Mv^2}{2k_B T}\right) dv, \tag{2.10}$$

where M is the atomic mass and T is the cell temperature in Kelvin. Here we can define $\sigma_v = \sqrt{\frac{k_B T}{M}}$, that is the standard deviation of the Gaussian distribution, and is linked to the most probable atomic velocity ($u = \sqrt{2}\sigma_v$).

Recalling equation 2.8, written in absence of broadening mechanisms, the line shape function g including Doppler effect is now given by a Gaussian function:

$$g(\omega_L, \omega_{ge}) = \sqrt{\frac{Mc^2}{2\pi k_B T \omega_{ge}^2}} \cdot \exp\left(-\frac{Mc^2(\omega_L - \omega_{ge})^2}{2k_B T}\right) = \\ = \frac{1}{\sqrt{2\pi}\sigma_D} \cdot \exp\left(-\frac{(\omega_L - \omega_{ge})^2}{2\sigma_D^2}\right) \tag{2.11}$$

where the coefficient σ_D represents the width of the Gaussian, defined as $\sigma_D = \sqrt{\frac{k_B T}{Mc^2}} \cdot \omega_{ge}$.

The extraction of the natural linewidth from a Doppler-broadened absorption profile requires Doppler-free spectroscopy techniques. Several methods can achieve sub-Doppler resolution, such as polarization spectroscopy [30] and modulation transfer spectroscopy [31]. Among these, saturated absorption spectroscopy (SAS) is widely used due to its experimental simplicity and robust performance [26]. The principles of SAS also form the basis for the two-photon absorption spectroscopy technique used in this work. The idea behind this method is to introduce a pump beam of higher intensity, counterpropagating with respect to the probe beam, to excite a specific transition. Since the two beams have the same frequency, atoms that are stationary relative to the laboratory frame are affected equally by both beams. In such conditions, the pump beam depletes the ground state population of stationary atoms and, consequently, the probe beam experiences less absorption at this frequency. This creates a narrow dip in the absorption profile, which shows up as a peak in the transmission spectrum..

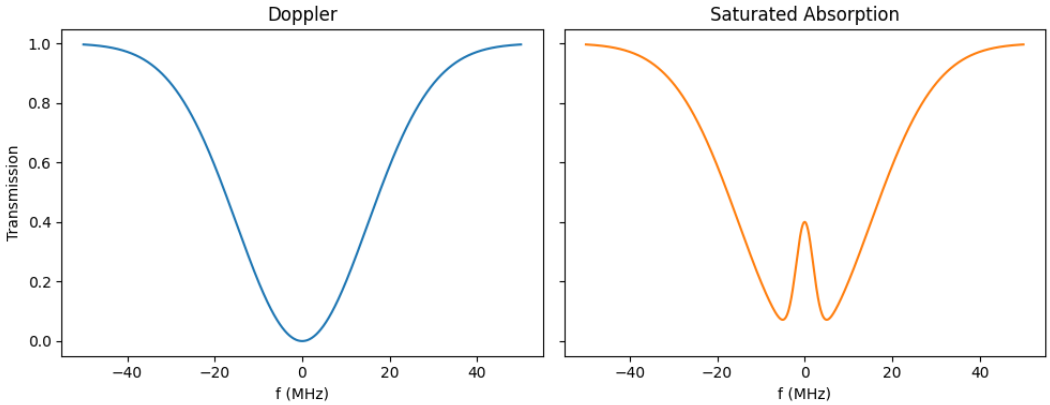

Fig. 2.5 Saturated Absorption Spectroscopy example.

In ideal conditions, the dip's width can match the natural linewidth of the transition and can be used as a Doppler-free spectroscopic tool to determine hyperfine atomic frequencies more precisely, with the possibility to lock the laser to a narrower feature (Figure 2.5).

2.2.6 Two-photon absorption spectroscopy

As discussed in the previous section, Doppler broadening arises from the thermal motion of the atoms in the vapor. More specifically, if $\bar{v}$ denotes the atomic velocity and $\bar{k}$ the wavevector of the incident light, the first-order Doppler shift is given by $\bar{k} \cdot \bar{v}$. When the direction of light propagation is reversed ($\bar{k} \rightarrow -\bar{k}$), this first-order Doppler shift changes sign. This principle is exploited in two-photon spectroscopy as well.

We now assume that the atoms can be excited to a state $|e\rangle$ (with energy E_e) from the ground state $|g\rangle$ (with energy E_g) by absorbing two photons. Using equation 2.9, the resonance condition for the absorption of two counterpropagating photons is then:

$$E_e - E_g = \hbar\omega_L \left(1 - \frac{v_z}{c}\right) + \hbar\omega_L \left(1 + \frac{v_z}{c}\right) = 2\hbar\omega_L, \tag{2.12}$$

in the approximation of non-relativistic atomic velocities $v_z \ll c$.

In the situation where both lasers operate at the same frequency (the degenerate case), the Doppler shift experienced by one photon is exactly opposite to that of the counter-propagating photon, independent of the atom's velocity. As a result, the combined frequency remains constant for all velocities, and atoms are excited only when the laser frequency equals half the transition energy. In this way, Doppler broadening is eliminated without the need for laser cooling. This mechanism differs from saturated absorption spectroscopy, where Doppler broadening is suppressed by isolating a single velocity class; in Doppler-free two-photon spectroscopy, atoms of all velocities contribute to the observed signal [32].

When the resonance condition is not satisfied, or if the two counter-propagating beams are not properly overlapped, atoms can no longer absorb a pair of photons traveling in opposite directions. Nevertheless, some atoms may still absorb two photons moving in the same direction, resulting in Doppler-broadened two-photon absorption. However, for a fixed laser frequency ω_l, only a single group of atoms with a specific velocity contributes to the Doppler-broadened signal, while, under condition 2.12, atoms across the entire velocity distribution take part in the resonance signal. Consequently, the Doppler-free two-photon absorption spectrum is observed

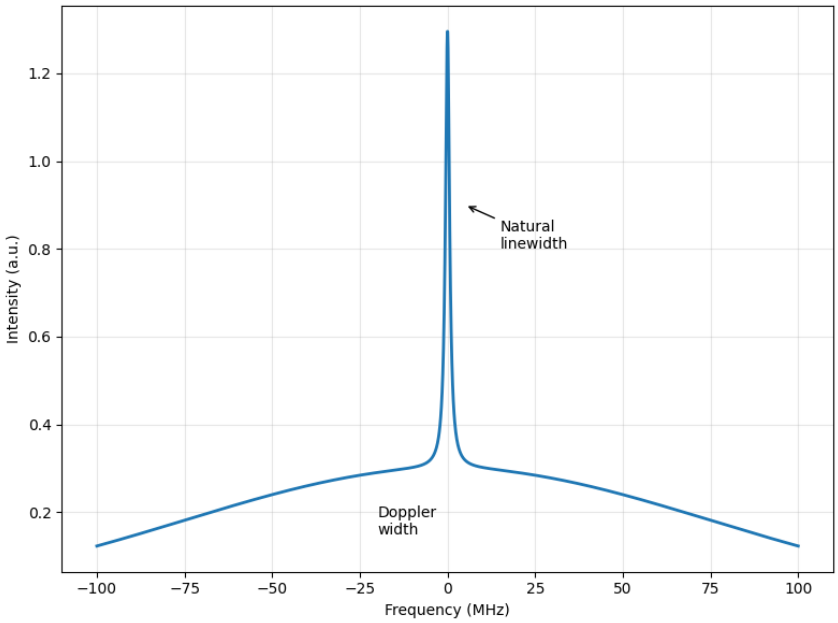

Fig. 2.6 Doppler-free two-photon absorption spectrum showing both the narrow Lorentzian peak and the broad Gaussian background.

as the sum of a high-intensity, narrow (natural linewidth) Lorentzian component and a low-intensity, broad Gaussian component (Figure 2.6, [33]).

An important requirement for implementing the Doppler-free two-photon scheme in high-resolution spectroscopy is that the laser linewidth should be on the order of (or smaller than) the natural linewidth of the transition under study. In spite of the traditionally high powers associated with two-photon excitation, the Doppler-free geometry strongly enhances the usable signal because all velocity classes contribute at resonance. Therefore, if the optical power is concentrated within a bandwidth smaller than the natural linewidth, appreciable excitation rates can be obtained even with moderate cw lasers.

In this regime, second-order perturbation theory predicts that the resonant two-photon transition probability scales with the square of the laser intensity [33]:

$$P_{\mathrm{ge}}^{(2)}(\mathrm{res}) = \frac{1}{\Gamma_{\mathrm{e}}}\left(\frac{3}{\pi}\frac{r_0\lambda_{\mathrm{gr}}\lambda_{re}}{\hbar c}\right)^2\left(\frac{P}{S}\right)^2\frac{\omega_{\mathrm{gr}}\omega_{re}}{\Delta\omega_r^2}f_{\mathrm{gr}}f_{re} \times \left|\left\langle J_{\mathrm{e}}\,1\,m_{\mathrm{e}}-q \mid J_r\,m_r\right\rangle\left\langle J_r\,1\,m_r-q \mid J_{\mathrm{g}}\,m_{\mathrm{g}}\right\rangle\right|^2, \tag{2.13}$$

In this expression, the index r labels a single dominant intermediate atomic state $|r\rangle$ of opposite parity to $|g\rangle$ and $|e\rangle$, which is coupled to both by allowed electric-dipole transitions. The laser frequency is chosen such that the one-photon detuning $\Delta\omega_r$ from $|r\rangle$ is large enough to avoid real population of this level (no stepwise excitation), yet small compared to the detunings of all other intermediate states so that $|r\rangle$ provides the main contribution to the second-order amplitude. In this picture, λ_{gr}, λ_{re}, ω_{gr}, ω_{re}, f_{gr}, and f_{re} are the wavelengths, angular frequencies, and oscillator strengths of the real one-photon transitions $|g\rangle \to |r\rangle$ and $|r\rangle \to |e\rangle$. $\Delta\omega_r$ quantifies how far the laser is detuned from the intermediate resonance and the last term shows the squared product of the Clebsch–Gordan coefficients, which weight the contribution of a specific magnetic sublevel $|r, J_r, m_r\rangle$ given the polarization component q of the light ($q = +1, 0, -1$ respectively for polarization σ^+, π, and σ^-).

Finally, the dependence $\propto 1/S^2$ shows that tighter focusing (smaller S parameter) increases the transition probability, provided that additional broadening effects remain negligible.

Chapter 3

Nonlinear Optics

In the broad context of atomic clocks, non-linear optics plays an important role since it provides access to atomic transitions that lie at wavelengths different from those of readily available lasers. In this work, conveniently, 778nm light, required for the rubidium two-photon transition, can be produced via second-harmonic generation (SHG) of 1556nm, which falls in the telecommunications C-band and allows the use of mature laser sources and erbium fiber frequency combs.

This chapter will briefly introduce the main concepts of Nonlinear Optics with an emphasis on Second Harmonic Generation. Readers seeking comprehensive treatments are referred to standard references that inform this chapter's presentation [34–36].

3.1 Introduction

Nonlinear optics investigates light–matter interactions in which the material response depends on the optical intensity, a regime that is the key for the generation and control of quantum states of light [37]. When an electromagnetic wave propagates in a medium, it induces a polarization that follows the space–time oscillations of the field; this polarization, in turn, radiates, providing the source of the emitted light. At sufficiently high field amplitudes, the response becomes nonlinear and the harmonic-oscillator (Lorentz) approximation must be extended to include anharmonic contributions. The invention of the laser in 1960 provided the necessary field

strengths to access such regimes, marking a practical breakthrough for nonlinear optics [38].

In the long history of optics, it was commonly assumed that optical media respond linearly:

$$P(t) = \varepsilon_0 \chi^{(1)} E(t), \tag{3.1}$$

where $P(t)$ is the induced macroscopic polarization, ε_0 is the vacuum permittivity and $\chi^{(1)}$ is the linear susceptibility of the medium.

However, experiments demonstrate that optical media do in fact exhibit non-linear behaviour, as exemplified by the following observations:

- The refractive index, and consequently the speed of light in a non-linear optical medium, does depend not only on frequency, but also on light intensity. This is a counterintuitive property, since it means that light itself modifies the properties of its propagation inside the medium. This effect was a breakthrough, discovered experimentally in 1961 by John Kerr, and is now known as the optical Kerr effect [39].
- The frequency of light is altered as it passes through a non-linear optical medium. This second effect puzzled physicist the most and it was demonstrated in 1961 by Peter Franken and coworkers [40]. That experiment is regarded as the birth of non-linear optics, occurring one year after the invention of the laser.

From these observations, a wide range of non-linear fascinating phenomena arised, many of which are exploited in modern technology: non-linear optics remains an actively developed field still today.

3.1.1 Anharmonic Oscillator Analogy

The Lorentz harmonic-oscillator model provides an accurate description of the linear optical response of atomic vapors, for which the induced polarization is proportional to the driving electric field:

$$\frac{d^2x}{dt^2} + \gamma\frac{dx}{dt} + \omega_0^2 x = -\frac{e}{m}E(t), \tag{3.2}$$

where x is the displacement of the electron from its equilibrium position, γ is the damping coefficient and the restoring force has the expression $F_A = -m\omega_0^2 x$ and it is associated to an harmonic potential energy:

$$F_A = -\frac{dU}{dx} \longrightarrow U(x) = \frac{1}{2}m\omega_0^2 x^2 \tag{3.3}$$

with ${\omega_0}^2 = \frac{k}{m}$, with k being the effective spring constant of the bound electron. While k is purely phenomenological in the classical model, in the quantum treatment it's connected to the energy separation between atomic discrete levels.

To understand non-linear phenomena, the Lorentz model can be extended by introducing anharmonicity in the restoring force acting on bound electrons (e.g., quadratically dependent on the displacement):

$$\frac{d^2x}{dt^2} + \gamma\frac{dx}{dt} + \omega_0^2 x + ax^2 = -\frac{e}{m}E(t) \tag{3.4}$$

In this case, the potential energy is anharmonic:

$$F_A = -\frac{dU}{dx} \longrightarrow U(x) = \frac{1}{2}m\omega_0^2 x^2 + \frac{1}{3}max^3 \tag{3.5}$$

Consequently, the solution of 3.4 deviates from a damped cosine/sine, leading to a non-linear relation between $x(t)$ and $E(t)$.

As a result, the material response ceases to be strictly linear and the polarization is no longer proportional to the field: the starting point of non-linear optics is indeed the non-linear dependence of the polarization $P(t)$ on $E(t)$.

3.1.2 Non-linear Optical Susceptibility

In practice, nonlinear terms are much smaller than the linear response, so nonlinear effects are observable only if the driving field is sufficiently strong. In these cases, it is convenient to decompose the polarization into linear and nonlinear parts. We start

the analysis by expanding the atomic polarization in powers of the electric field (like in a Taylor expansion):

$$P(t) = \varepsilon_0 \left(\chi^{(1)} E(t) + \chi^{(2)} E^2(t) + \chi^{(3)} E^3(t) + ... \right) \tag{3.6}$$

where $\chi^{(1)}$ is the linear susceptibility, $\chi^{(2)}$ and $\chi^{(3)}$ are the second and third order non-linear susceptibilities.

In this introduction, for a simplified treatment, we consider several assumptions:

(1) The material is isotropic, homogeneous and lossless. All the optical susceptibility terms are real and scalar quantities, independent of space (in a more accurate description, the non-linear susceptibilities are not numbers, but tensors).

(2) Light is linearly polarized and propagating along the z direction. The only interesting components of the atomic polarization are along the linear polarization axis.

(3) The linear and non-linear susceptibilities are "non-dispersive", meaning neither dispersion nor absorption is taken into account.

Under assumption (3), $\chi^{(1)}$, $\chi^{(2)}$ and $\chi^{(3)}$ are not functions of ω in the frequency domain. Thus we write:

$$\hat{P}(\omega) = \hat{P}_L(\omega) + \hat{P_{NL}}(\omega) \tag{3.7}$$

with

$$\hat{P}_L(\omega) = \varepsilon_0 \hat{\chi}^{(1)} E(\omega) \tag{3.8}$$

and

$$\hat{P_{NL}}(\omega) = \varepsilon_0 \left(\hat{\chi}^{(2)} E^2(\omega) + \hat{\chi}^{(3)} E^3(\omega) + ... \right) \tag{3.9}$$

where "$\hat{\chi}$" indicates the Fourier transform.

In general, P and ε may depend on the position inside the medium. Therefore, exploiting again (3), we can rewrite 3.6 in the time domain as:

$$P(\bar{r},t) = \varepsilon_0 \left(\chi^{(1)} E(\bar{r},t) + \chi^{(2)} E^2(\bar{r},t) + \chi^{(3)} E^3(\bar{r},t) + ... \right) = P_L(\bar{r},t) + P_{NL}(\bar{r},t) \tag{3.10}$$

A practical treatment typically retains only the lowest non-vanishing orders: $\chi^{(1)}$ (linear term), $\chi^{(2)}$ (responsible for e.g. second harmonic generation and Optical parametric amplification) and $\chi^{(3)}$ (responsible for e.g. self-focusing, self-modulation). All higher contributions are usually much smaller and can be safely neglected for the interpretation of experiments. In many materials $\chi^{(3)} << \chi^{(2)}$, but there exist materials in which the second-order susceptibility (and in general all even orders) is null. These are called centrosymmetric. where inversion symmetry is realized, i.e. material properties are not altered under a transformation: $\bar{r} \to -\bar{r}$.

This means that the macroscopic polarization must reverse under field reversal, i.e. $P(E) = -P(-E)$. Consequently, in the Taylor expansion of $P(E)$ all even-order terms vanish in the electric-dipole approximation: $\chi^{(2)} = 0$.

Typically, all liquids, gases and amorphous solids (e.g., glass) are centrosymmetric, so they have a strong contribution of third-order nonlinearity. Usual values of the second-order nonlinear coefficient $\frac{\varepsilon_0 \chi^{(2)}}{2}$ are on the order of $10^{-24} - 10^{-21} C/V^2$ while third order coefficients $\frac{\varepsilon_0 \chi^{(3)}}{4}$ are on the order of $10^{-34} - 10^{-29} C/V^3$ (the values and the corresponding notation are taken from [41]). As a consequence these non-linear correction terms become relevant only when the electric fields are of the order of $10^5 - 10^8 V/m$.

Table 3.1 summarizes some examples of second- and third-order nonlinear susceptibilities, with notation and values taken from [36].

Material	$\chi_{ij}^{(2)}\,(pm/V)$
βBaB_2O_4	$\chi_{22}^{(2)} = 1.1$
$GaAs$	$\chi_{36}^{(2)} = 185$
$LiNbO_3$	$\chi_{22}^{(2)} = -15$
$CdGeAs_2$	$\chi_{22}^{(2)} = 117.5$

Material	$\chi^{(3)}\,(m^2/V^2)$
$GaAs$	1.4×10^{-18}
Si	2.8×10^{-18}

Table 3.1 Examples of second- and third-order nonlinear susceptibilities.

3.2 Second Harmonic Generation Theory

3.2.1 Wave Equation and Coupled Wave Theory

We now discuss in details the physical consequences of a nonlinear polarization. To do so, we need to start as always from canonical optics from the Maxwell's equations inside the medium. Supposing to be far from conduction currents and free charges, the wave equation in a non-linear medium tells:

$$\nabla^2 E(\bar{r},t) = \mu_0 \frac{\partial^2 D(\bar{r},t)}{\partial t^2} = \mu_0 \varepsilon_0 (1+\chi^{(1)}) \frac{\partial^2 E(\bar{r},t)}{\partial t^2} + \mu_0 \frac{\partial^2 P_{NL}(\bar{r},t)}{\partial t^2} \tag{3.11}$$

where $P_L(\bar{r},t) = \varepsilon_0 \chi^{(1)} E(\bar{r},t)$ and $1+\chi^{(1)} = n^2$ (linear refractive index).

More compactly:

$$\nabla^2 E(\bar{r},t) - \frac{1}{v_g} \frac{\partial^2 E(\bar{r},t)}{\partial t^2} = \frac{1}{\varepsilon_0 c^2} \frac{\partial^2 P_{NL}(\bar{r},t)}{\partial t^2} \tag{3.12}$$

where $v_g = \frac{c}{n}$ is the group velocity of light in the medium.

Equation 3.12 is the nonlinear Maxwell equation governing the interaction of an electromagnetic wave with a nonlinear medium. In the weak-scattering Born picture, one treats the nonlinear polarization driven by the incident field as a source term that radiates new frequency components. While this provides intuitive insight into

frequency generation, it is not so accurate for quantitative propagation problems. In what follows, the more complex and rigorous coupled-wave theory is adopted.

To solve 3.12 apart from the assumptions (1), (2) and (3) considered in Section 3.1.1, we also introduce:

(4) Plane Wave Approximation

(5) Slowly Varying Envelope Approximation (SVEA)

With assumption (4), the field is modeled as a plane wave and represented, by the Fourier Theorem, as a superposition of monochromatic components at frequencies ω_p, all propagating along z. In complex notation:

$$E(z,t) = \frac{1}{2}\sum_p \left(E_p(z) e^{i(k_p z - \omega_p t)} + c.c. \right) \tag{3.13}$$

where $k_p = n\frac{\omega_p}{v_g}$ is the propagation constant at frequency ω_p (here $v_g = v$ from the considered assumptions).

Still, 3.12 cannot be easily solved. Assumption (5) supposes that the field envelope varies slowly in z as compared to the wavelength of the carrier wave $\lambda_p = \frac{2\pi}{k_p}$. This allows to neglect higher-order derivatives of the envelope with respect to z:

$$\left| \frac{\partial^2 E_p(z)}{\partial z^2} \right| << \left| k_p \frac{\partial E_p(z)}{\partial z} \right| \tag{3.14}$$

Applying approximations (4) and (5) to the basic Boltzmann equation (3.12), replacing $E(\bar{r},t)$ with 3.13, we obtain:

$$\sum_p \frac{1}{2} \left(2ik_p \frac{\partial E_p(z)}{\partial z} e^{i(k_p z - \omega_p t)} + cc \right) = \frac{1}{\varepsilon_0 c^2} \frac{\partial^2 P_{NL}(z,t)}{\partial t^2} \tag{3.15}$$

Writing $P_{NL}(z,t) = \varepsilon_0 \chi^{(2)} E(z,t)^2 + \varepsilon_0 \chi^{(3)} E(z,t)^3$ and matching equal-frequency terms on both sides, this equation is equivalent to a set of nonlinear ordinary differential equations for the envelopes at each different frequency ω_p, describing how each spectral component evolves along z inside the medium. In other words, waves

are coupled through nonlinearity inside the medium and 3.15 expresses how the "amplitude" of input frequencies decreases while new components grow.

3.2.2 Quadratic Non-Linearity: Second Harmonic Generation

In this section, we focus on the solution of 3.15 for the specific case of Second Harmonic Generation, without entering in the details of cubic nonlinearity. The effect of Second Harmonic Generation can be explained using the second-order nonlinearity and by simply assuming to have a monochromatic plane wave as input:

$$\begin{cases} E(z,t) = \frac{1}{2}\left(E_1(z)e^{i(k_1 z-\omega_1 t)} + c.c.\right) \\ P_{NL}(z,t) = \varepsilon_0 \chi^{(2)} E^2(z,t) \end{cases} \tag{3.16}$$

Thus:

$$\begin{aligned} P_{NL}(z,t) &= \varepsilon_0 \chi^{(2)}\left(\tfrac{1}{2}E_1(z)e^{i(k_1 z-\omega_1 t)} + \tfrac{1}{2}E_1^*(z)e^{-i(k_1 z-\omega_1 t)}\right)^2 \\ &= \varepsilon_0 \chi^{(2)}\left(\tfrac{1}{4}E_1^2(z)e^{2i(k_1 z-\omega_1 t)} + \tfrac{1}{4}E_1^{*2}(z)e^{-2i(k_1 z-\omega_1 t)} + \tfrac{1}{2}|E_1(z)|^2\right) \\ &= P_{NL,2\omega_1}(z,t) + P_{NL,DC}(z,t) \end{aligned} \tag{3.17}$$

Therefore,

$$P_{NL,2\omega_1}(z,t) = \frac{1}{2}\varepsilon_0 \chi^{(2)} Re\left[E_1^2(z)e^{2i(k_1 z-\omega_1 t)}\right] \tag{3.18}$$

describes the second harmonic generation at frequency $2\omega_1$ and

$$P_{NL,DC}(z,t) = \frac{1}{2}\varepsilon_0 \chi^{(2)} |E_1(z)|^2 \tag{3.19}$$

is a DC term that gives rise to optical rectification (OR), i.e. the generation of a static electric field inside the medium.

Second Harmonic Generation can be understood as the combination of two photons at frequency ω_1 to produce a single photon at frequency $2\omega_1$. This fre-

quency up-conversion process conserves energy and allows the generation of light at wavelengths that may be inaccessible to conventional laser sources.

We call now $E_1(z)$ the envelope of the electric field at frequency ω_1 and $E_2(z)$ the envelope of the electric field at frequency $\omega_2 = 2\omega_1$. Inserting the two frequencies in 3.15, we obtain:

$$2i\left(k_1 Re\left[\frac{\partial E_1(z)}{\partial z}e^{(k_1 z-\omega_1 t)}\right]+k_2 Re\left[\frac{\partial E_2(z)}{\partial z}e^{(k_2 z-\omega_2 t)}\right]\right)=\frac{1}{\varepsilon_0 c^2}\frac{\partial^2 P_{NL}(z,t)}{\partial t^2} \tag{3.20}$$

Focusing only on the non linear polarization term regarding SHG (3.18) and setting $\omega_2 = 2\omega_1$ we get the equation describing the evolution of the second harmonic field $E_2(z)$:

$$e^{i(k_2 z-\omega_2 t)}\frac{\partial E_2(z)}{\partial z}=\frac{1}{2ik_2\varepsilon_0 c^2}\frac{\partial^2 P_{NL,2\omega_1}(z,t)}{\partial t^2} \tag{3.21}$$

By deriving twice $P_{NL,2\omega_1}(z,t)$ and simplifying we obtain:

$$\frac{\partial E_2(z)}{\partial z}=i\frac{\omega_2}{4n_2 c}\chi^{(2)}E_1^2(z)e^{i\Delta k z} \tag{3.22}$$

where $\Delta k = 2k_1 - k_2$ is the phase mismatch parameter.

For the model to be self-consistent another equation must be written for the electric field envelope E_1 at frequency ω_1 [1]:

$$\frac{\partial E_1(z)}{\partial z}=i\frac{\omega_1}{2n_1 c}\chi^{(2)}E_1^*(z)E_2(z)e^{-i\Delta k z} \tag{3.23}$$

Thus, by combining the two:

$$\begin{cases}\frac{\partial E_1(z)}{\partial z}=i\frac{\omega_1}{2n_1 c}\chi^{(2)}E_1^*(z)E_2(z)e^{-i\Delta k z}\\ \frac{\partial E_2(z)}{\partial z}=i\frac{\omega_2}{4n_2 c}\chi^{(2)}E_1^2(z)e^{i\Delta k z}\end{cases} \tag{3.24}$$

[1] This comes from considering $E(z,t)$ equal to the sum of monochromatic wave at frequency ω_1 and a monochromatic wave at frequency ω_2. For further details, see e.g. [35]

The first order non-linear ODE are solved with initial conditions at the input face $z = 0$. Obviously $E_2(0) = 0$ as only the fundamental wave is incident on the medium at $\omega = \omega_1$, therefore $E_1(0)$ is fixed by the external source and is typically large.

Considering a non linear medium of length L, in the hypothesis of undepleted pump (Assumption (6)), i.e. $E_1(z) \approx E_1(0)$, the two equations are completely decoupled. The envelope of the electric field at frequency ω_2 at its end L is:

$$E_2(L) = i\frac{\omega_2}{4n_2c}\hat{\chi}^{(2)}E_1^2(0)\int_0^L e^{i\Delta kz}dz = i\frac{\omega_2}{4n_2c}\hat{\chi}^{(2)}E_1(0)\frac{1}{\Delta k}\left(e^{i\Delta kL}-1\right) \tag{3.25}$$

From which, calling $I_2 = I_2(L)$ and $I_1 = I_1(0)$ we obtain

$$I_2 = |E_2(L)|^2 = \left(\frac{\omega_2^2}{4n_2c}\hat{\chi}^{(2)}\right)^2 I_1^2L^2 sinc^2\left(\frac{\Delta kL}{2}\right) \tag{3.26}$$

Collecting all the constants in a single one $\kappa_2 = \left(\frac{\omega_2}{4n_2c}\hat{\chi}^{(2)}\right)^2$, we have:

$$I_2 = \kappa_2 I_1^2L^2 sinc^2\left(\frac{\Delta kL}{2}\right) \tag{3.27}$$

The conversion efficiency exhibits a $sinc^2$-type dependence on the phase mismatch, so for a given interaction length the maximum efficiency occurs for the exact phase matching condition:

$$\Delta k = 0 \longrightarrow 2k_1 = k_2 \tag{3.28}$$

When phase matching is not satisfied (or only weakly satisfied), the efficiency is very low and the behavior approaches the linear case. If the second-harmonic intensity is plotted versus propagation distance within the medium for different values of Δk, one obtains the characteristic quadratic growth for near-zero mismatch and oscillatory exchange for finite mismatch (Figure 3.1b).

For $\Delta k \neq 0$ the intensity oscillates with a period $L_c = \frac{2\pi}{\Delta k}$, called coherence length. This means that after a propagation distance L_c, the intensity of the second harmonic goes back to zero, i.e. the process is not efficient at all.

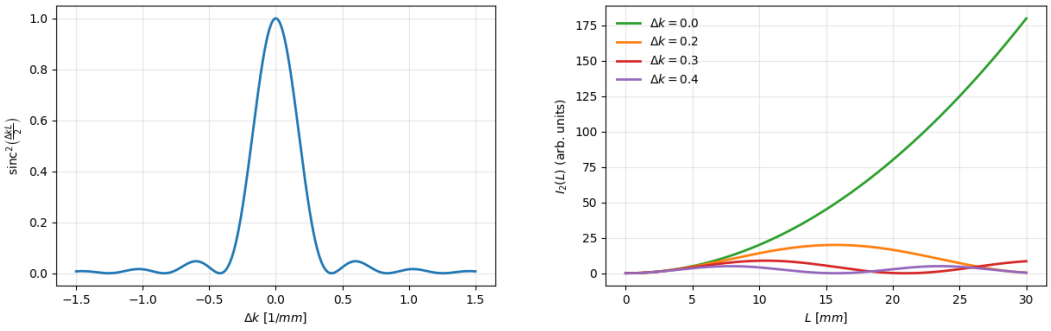

(a) (b)

Fig. 3.1 (a) $sinc^2$ dependence of the SHG intensity on the phase mismatch. (b) SHG intensity versus propagation distance L for different values of Δk.

3.3 Phase Matching

This section outlines the experimental strategies to achieve phase matching for maximizing the SHG conversion efficiency. The discussion focuses on collinear Type I phase matching in three-wave mixing, where all interacting waves propagate along the same direction.

3.3.1 Collinear Three Wave Mixing

For non-dispersive materials, the condition $\Delta k = 0 \equiv k_1 + k_2 - k_3 = 0$ becomes:

$$\frac{n\omega_1}{c} + \frac{n\omega_2}{c} = \frac{n\omega_3}{c} \tag{3.29}$$

where $n = n(\omega_i)$ is the same refractive index for each frequency involved in the process. Simplifying, 3.29 is recasted as the energy conservation law:

$$\omega_1 + \omega_2 = \omega_3 \tag{3.30}$$

Because real materials are dispersive, the refractive index depends on frequency: $n_i = n(\omega_i)$. As a consequence, the phase matching condition now reads:

$$n_1\omega_1 + n_2\omega_2 = n_3\omega_3 \tag{3.31}$$

3.31 is independent of the frequency matching condition and both constraints must be satisfied. For the case of Second Harmonic Generation, we can set $\omega_1 = \omega_2$ and $\omega_3 = 2\omega_1$ and 3.31 becomes:

$$2n_1\omega_1 = n_3 \cdot 2\omega_1 \longrightarrow n_1 = n_3 \tag{3.32}$$

or, equivalently, $n(\omega_1) = n(2\omega_1)$.

3.3.2 Birefringence and Type I phase matching

In isotropic material under normal dispersion, collinear, same-polarization SHG generally cannot satisfy $n(2\omega_1) = n(\omega_1)$, so exact phase matching is not available in that simple configuration. In fact, a wave travelling through an isotropic medium experiences the same refractive index regardless of its polarization and propagation direction. In this case, defining $n = \sqrt{1+\chi^{(1)}}$, the dielectric tensor $\varepsilon_{ij} = 1 + \chi^{(1)}_{ij}$ is diagonal with equal entries.

In anisotropic media this is not generally the case, as ε_{ij} contains distinct principal values and, in a generic laboratory frame, off-diagonal components. However, for lossless (non-absorbing) materials, ε_{ij} is symmetric and can be diagonalized, corresponding to a change from the laboratory frame to the material's dielectric coordinates. In that frame, a uniaxial crystal has the dielectric tensor

$$\varepsilon = diag(\varepsilon_o, \varepsilon_o, \varepsilon_e) \tag{3.33}$$

where ε_o and ε_e are the ordinary and extraordinary dielectric constants, corresponding to refractive indices $n_o = \sqrt{\varepsilon_o}$ and $n_e = \sqrt{\varepsilon_e}$. Thus, two principal axes share the same refractive index n_o, while the third axis has a distinct index n_e and defines the optic axis.

The dependence of the refractive index on the polarization and propagation direction of light is called birefringence and it represents the key ingredient to realize phase matching. By choosing the propagation direction relative to the optic axis (i.e., tuning the angle θ), birefringence can compensate material dispersion provided the appropriate index relation is satisfied:

$$n_e(\theta, 2\omega_1) = n_o(\omega_1) \tag{3.34}$$

This configuration corresponds to Type I phase matching, where the two fundamental waves at ω_1 are ordinary polarized and the second harmonic wave at $2\omega_1$ is extraordinary polarized ("ooe" configuration, see Figure 3.2). As indicated by 3.34, the ordinary refractive index at a given wavelength is fixed (by the material's Sellmeier relation), whereas the extraordinary refractive index depends on the propagation angle θ relative to the optic axis. Such angular dependence is expressed as:

$$\frac{1}{n_e^2(\theta)} = \frac{\cos^2(\theta)}{n_o^2} + \frac{\sin^2(\theta)}{n_e^2} \tag{3.35}$$

Here, $n_e \equiv n_e(90°)$ is set by the Sellmeier relation as well. From 3.35, one finds $n_e(0°) = n_o$: when light propagates along the optic axis, the refractive index is polarization-independent and birefringence vanishes. Uniaxial crystals are so called since they possess a single optic axis.

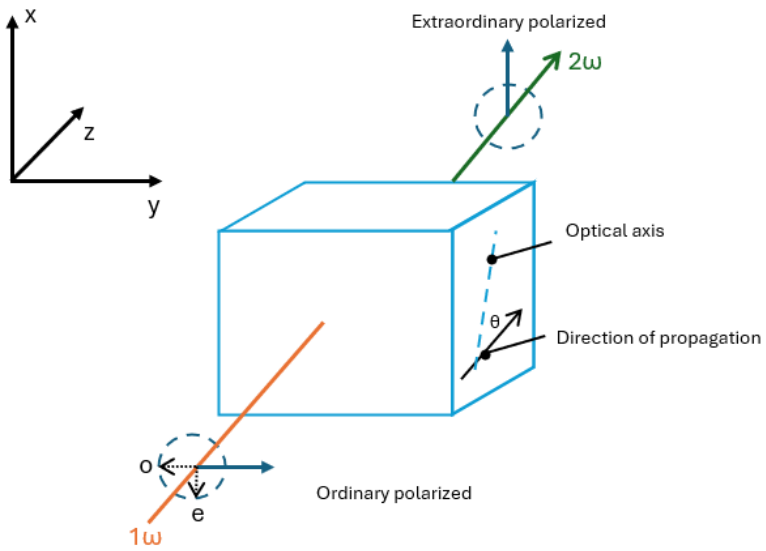

Fig. 3.2 Type I "ooe" phase matching in a uniaxial crystal.

Finally, a practical consequence of birefringent phase matching is spatial walk-off: for the extraordinary wave, the Poynting vector (energy flow) is not collinear

with the wave vector, forming a walk-off angle ρ. As a result, the ordinary and extraordinary beams gradually separate transversely as they propagate, reducing their spatial overlap and the effective interaction length. This phenomenon degrades the SHG efficiency and must be accounted for during the crystal selection, particularly regarding crystal length and walk-off angles.

3.4 SHG conversion efficiency for gaussian beams

In the previous sections, the theory of SHG was developed under the plane wave approximation. However, in real experiments, the incoming light is typically not a perfect plane wave but rather a Gaussian beam (described in more details in Section 4.1.2). This has important implications for the efficiency of the SHG process.

3.4.1 The Boyd-Kleinman Function

The canonical treatment of SHG with focused Gaussian beams was developed by Boyd and Kleinman (1968) [42]. Their analysis yields a closed-form expression for the second-harmonic output power:

$$P_{2\omega_1} = KP_{\omega_1}^2 Lk_1 e^{-\alpha L} h(\sigma, B, \kappa, \xi, \mu) \tag{3.36}$$

where

- $K = \frac{128\omega_1^2\pi^2}{c^3 n(\omega_1)^2 n(\omega_2)} d_{eff}^2$, is a constant depending on the material properties (d_{eff} is the effective non-linear coefficient, related to $\chi^{(2)}$).
- P_{ω_1} is the input power at frequency ω_1.
- L is the crystal length.
- k_1 is the propagation constant at frequency ω_1.
- α is the "total" absorption coefficient inside the medium, defined as $\alpha = \alpha(\omega_1) + \frac{1}{2}\alpha(\omega_2)$.

The function $h(\sigma,\beta,\kappa,\xi,\mu)$ encapsulates the full dependence of $P_{2\omega_1}$ on the optimizable parameters σ, μ, ξ representing, respectively, the phase mismatch, focal position, and strength of focusing. In addition, h depends on the birefringent parameter β and absorption κ. It can be expressed as a double integral:

$$h(\sigma,\beta,\kappa,\xi,\mu) = \frac{1}{4\xi}\int\int_{-\xi(1-\mu)}^{\xi(1+\mu)} d\tau d\tau' \frac{e^{[-\kappa(\tau+\tau')+i\sigma(\tau-\tau')-\beta^2(\tau-\tau')^2]}}{(1+i\tau)(1-i\tau')} \tag{3.37}$$

where

- $\sigma = \frac{b\Delta k}{2}$. $b = \frac{2\pi n(\omega_1)w_0^2}{\lambda}$ is the confocal parameter and w_0 is the beam waist (radius) inside the medium (Figure 4.3).
- $\mu = \frac{L-2f}{L}$, with f being the position of the beam waist relative to the input facet of the medium.
- $\beta = B\sqrt{\xi}$ where $B = \rho\frac{\sqrt{Lk_1}}{2}$ is the double refraction parameter accounting for ρ, the walk off angle.

Finally $\xi = \frac{L}{b}$ and $\kappa = \frac{\alpha b}{2}$.

The Boyd-Kleinman function $h(\sigma,\beta,\kappa,\xi,\mu)$ can be numerically evaluated for different values of its parameters. Of particular interest is the case of no absorption and focus of the beam in the center of the crystal, i.e. $\kappa = \mu = 0$. Once the phase matching condition is optimized and σ is fixed to an optimum value, β can be related to B and the function can be treated by varying B and ξ. Figure 3.3 shows the behavior of $h(B,\xi)$ for different values of its optimizable parameters.

Each curve of Figure 3.3 exhibits a single maximum that defines the optimal focusing $\xi(B)$. As the walk-off parameter B increases, the peak value decreases, indicating that walk-off degrades SHG efficiency. At the same time, increasing the focus at the center of the crystal is beneficial up to a certain threshold. Beyond that, further increasing ξ reduces the effective interaction length within the medium and lowers efficiency of the SHG process. Boyd and Kleinman found that the optimum value of ξ lies in the range $1.392 < \xi < 2.84$.

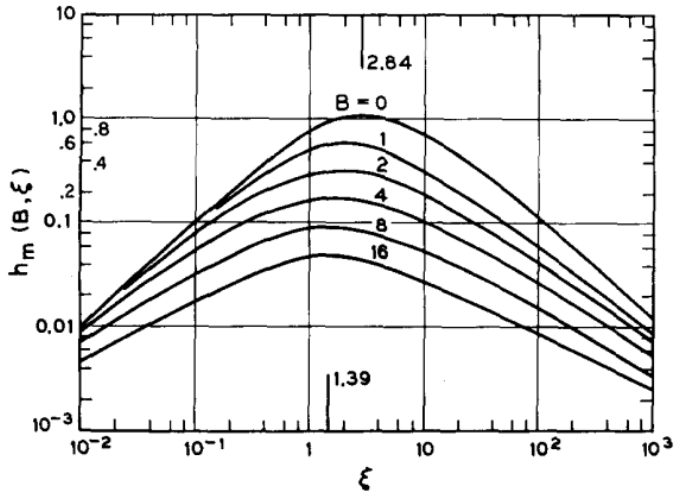

Fig. 3.3 $h(B,\xi)$ as a function of ξ for several values of the double refraction parameter B. Vertical lines indicate optimum focusing in the limits of small and large B. Reproduced with permission from Boyd and Kleinman, J. Appl. Phys. 39, 3597 (1968). © 1968 American Institute of Physics.

3.5 Crystal choice for SHG

In the next sections, the performance of the main crystalline materials used for Second Harmonic Generation is evaluated, focusing on the case of single-pass, continuous wave frequency conversion according to the theoretical framework introduced in Section 3.4

The material choice naturally prioritizes a large effective nonlinear coefficient d_{eff}, minimal spatial and temporal walk-off, and low optical loss across the interacting wavelengths. In practice, performances are constrained by additional factors such as manufacturable crystal dimensions (aperture and length), AR-coating quality and tolerances. The optimal device, therefore, balances theoretical conversion efficiency against the bounds set by crystal growth quality and the sizes that can be procured.

3.5.1 Borate Non Linear Optical Crystals

As explained in Section 3.3, birefringence is essential for phase matching in nonlinear crystals. The birefringent crystals that are now evaluated are BBO (BaB_20_4), LBO (LiB_30_5), CLBO ($CsLiB_6O_{10}$), and BIBO (BiB_3O_6), chosen because of their

wide transparency windows and broad SHG phase-matchable ranges, which make them well suited for harmonic generation across a wide spectrum. Here, we focus specifically on frequency doubling from 1556*nm* to 778*nm*.

The evaluation starts by systematically determining the optical properties needed to calculate the output power using the derived theoretical model. For this purpose, the calculations are performed considering equation 3.36, which is rewritten in the International System of Units in Section 4.1.4. Characteristic crystal parameters, such as the Sellmeier equations (used to derive refractive indices and phase matching angles), effective nonlinear coefficients (d_{eff}), and absorption coefficients (α) come from literature and vendor specifications [43, 44]. After finding the refractive indices, the spatial walk-off angle (ρ) is calculated using the angular derivative relationship [45]:

$$\rho = -\frac{1}{ne} \cdot \frac{dn(\theta)}{d\theta} \tag{3.38}$$

These parameters are listed in Table 3.2, with some values being obtained or verified using the SNLO nonlinear optics software [46].

Table 3.2 Optical parameters for the nonlinear crystals used in CW SHG at a fundamental wavelength of $\lambda_{\text{in}} = 1556$ nm.

Parameter	**BBO**	**LBO**	**CLBO**	**BIBO**
$n(\omega_1) = n(\omega_2)$	1.63	1.60	1.48	1.73
ρ (mrad)	45.21	5.73	27.43	30.45
d_{eff} (pm/V)	2.10	0.80	0.35	2.70
$\alpha(\omega_1)$ $(\%/cm^{-1})$	≤ 0.1	≤ 0.1	≤ 0.03	≤ 0.1
$\alpha(\omega_2)$ $(\%/cm^{-1})$	≤ 0.1	≤ 0.3	≤ 0.1	≤ 0.1
θ_{PM} (deg)	19.8	90	28.3	10.9
ϕ_{PM} (deg)	90	9.8	90	0.0

BBO and CLBO are uniaxial crystals, and the phase-matching configuration considered for these materials is Type I with an "ooe" polarization scheme. Similarly, the same configuration was considered for LBO and BIBO, which are biaxial crystals: for LBO, the phase-matching is analyzed in the XY plane, while for BIBO it is considered in the XZ plane. From the data presented, BIBO emerges as the most promising crystal for continuous-wave SHG at 1556 nm due to its higher effective second-order nonlinear coefficient. However, research literature has reported that

BIBO can exhibit certain instabilities under high incident powers during the SHG process [47]. Following BIBO, BBO is the next most efficient nonlinear material considered here, balancing good nonlinear efficiency with more established operational stability and keeping low absorption coefficients.

To identify the maximum theoretical efficiency each crystal can provide in the CW regime, the output power is calculated for different crystal lengths (L) while optimizing the laser focusing condition ξ. By evaluating different (L, ξ) combinations, we obtain the trends shown in Figure 3.4 for an input power $P_{in} = 2W$. To avoid redundancy, the plots presented correspond to BBO, which is representative of the behavior observed for all the considered crystals.

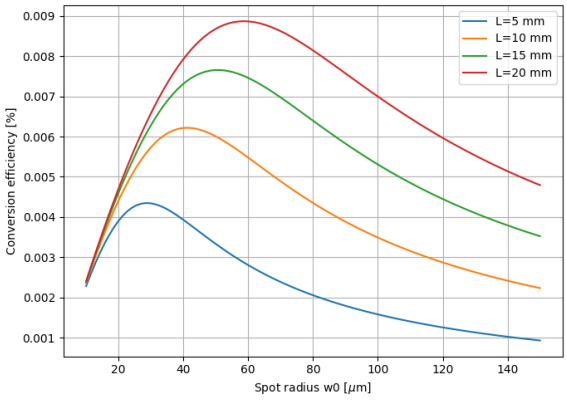

(a)

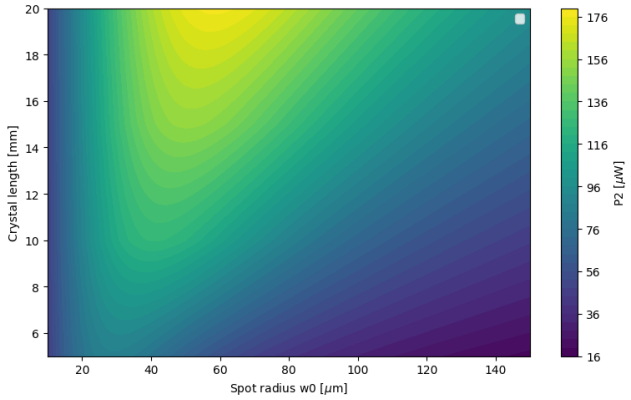

(b)

Fig. 3.4 (a) Conversion efficiency of BBO as a function of the beam waist radius inside the crystal, shown for various crystal lengths. (b) BBO Power heatmap varying crystal length and beam spot radius.

Figure 3.4a clearly illustrates the influence of the Boyd-Kleinman function h, since varying the beam spot radius outside the optimal range for ξ results in a significant reduction in SHG efficiency. It is also evident that increasing the crystal length enhances both the conversion efficiency and the output powers, within the practical length range typically produced by manufacturers. However, the benefits of increased crystal length must be balanced against cost considerations and increased sensitivity to local temperature variations: phase matching has to be maintained over a larger length, and eventually this will become difficult, particularly in a crystal oven. At the same time, greater values of L lead to a higher value of B, indicating an enhanced walk-off effect. This could be detrimental especially in pulsed operational regimes while, as shown in Figure 3.4a, its impact does not materially limit the results reported here for single-pass SHG generation.

By setting the crystal length, it's possible to make a comparison between the performances of the different crystals (Figure 3.5).

As expected, the BIBO crystal demonstrates the highest performance, followed by BBO. The LBO crystal exhibits a performance close to that of BBO, with an interesting trend of reaching comparable efficiency when the crystal length approaches 20 mm. This behavior can be attributed to the differences in walk-off angles between the crystals, which favor LBO for longer interaction lengths compared to BBO. On the other hand, CLBO produces significantly lower output power within this wavelength range.

In general, the single-pass SHG power and conversion efficiencies remain relatively low. For this reason, intracavity frequency doubling represents a fundamental enhancement strategy: by integrating these crystals within an optical cavity, the circulating power can be significantly increased, improving the output power and conversion efficiency. However, this approach introduces additional constraints on the crystal design, since the crystal length must be carefully matched to the cavity length to achieve an optimal focusing parameter ξ for efficient SHG. Moreover, residual reflections at the surfaces of the crystal must be minimized to keep negligible intracavity losses, which represent one of the greatest factor that reduces the overall SHG efficiency (see Section 4.2.1).

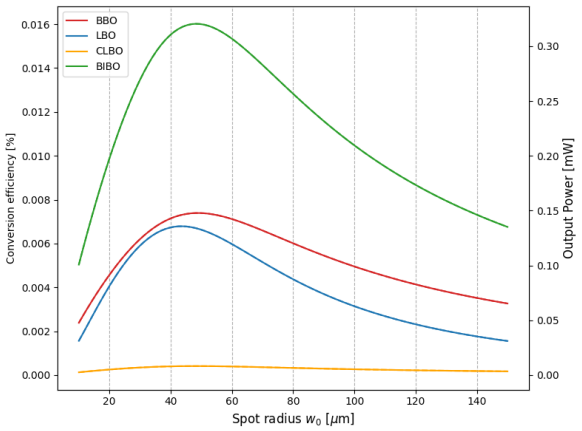

(a)

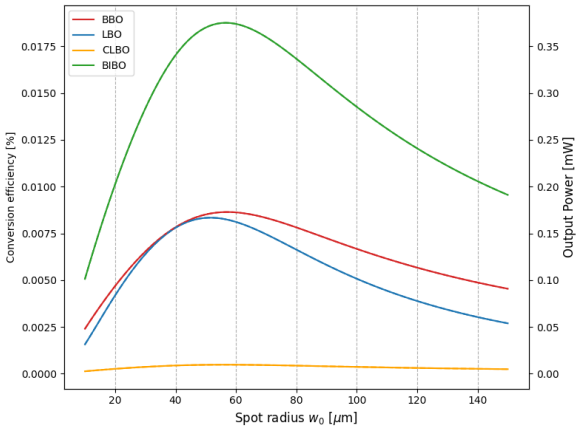

(b)

Fig. 3.5 Crystals SHG conversion efficiency and output generated power for $P_{in} = 2W$ and a) $L = 15mm$ and b) $L = 20mm$

3.5.2 Periodically Poled KTP Crystal

Even if it is not part of this work tractation, quasi-phase-matching offers a practical alternative to conventional birefringent phase-matching by periodically modulating the nonlinear susceptibility in a crystal. The process resets the phase difference between interacting waves every time it accumulates to π, maintaining constructive energy transfer from the fundamental wave to the second harmonic. Among the various materials, periodically poled potassium titanyl phosphate (PPKTP) stands out as a representative choice for SHG applications due to its relatively large effective nonlinear coefficient and a high damage threshold, which together ensure high SHG conversion efficiency.

The simplified Boyd–Kleinman function of Figure 3.3 can be applied to periodically poled materials, since the theory does not depend on how the phase-matching condition is satisfied. In this case, the 1rst-order periodic inversion introduces a factor $2/\pi$ in the reduction of d_{eff} [48]. Considering the non-linear coefficient $d_{33} = 16.9pm/V$ [49, 50], the proper value under analysis is found to be $d_eff = \frac{2d_{33}}{\pi} = 10.76pm/V$. At the same time, the treatment can be made considering B=0 [51, 52].

The conversion efficiency and output power results for the Periodically Poled KTP are reported in Figure 3.6.

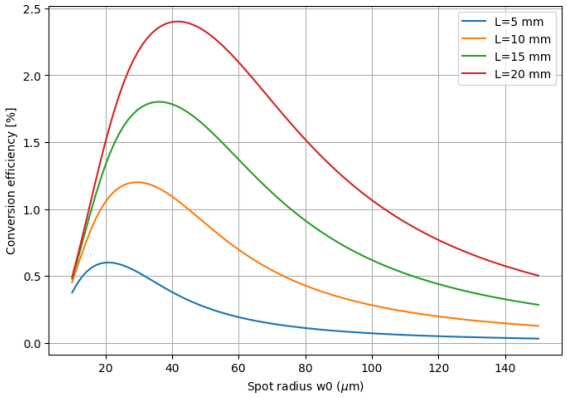

(a)

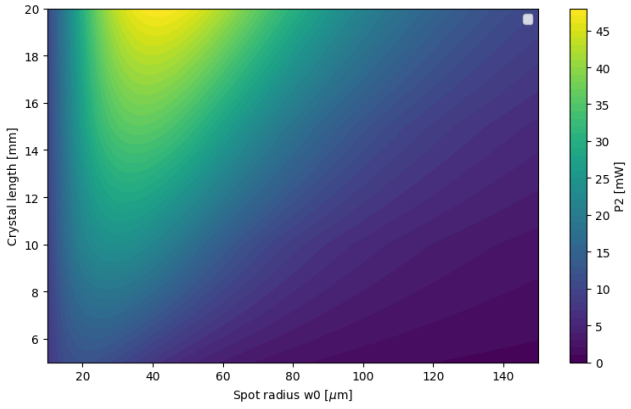

(b)

Fig. 3.6 (a) Conversion efficiency of PPKTP as a function of the beam waist radius inside the crystal, shown for various crystal lengths. (b) PPKTP Power heatmap varying crystal lenght and beam spot radius.

The theoretical results show a conversion efficiency exceeding 2% without requiring an optical cavity (consistent with previous experimental works [53, 54]),

highlighting PPKTP as a highly effective crystal for SHG at this wavelength, outperforming other borate crystals.

Although a Periodically Poled crystal like PPKTP achieves high efficiency through Quasi-Phase Matching, its advantage is linked to a permanently set poling period (Λ) tailored to a single fundamental wavelength. As a result, once created for a specific Second Harmonic Generation process, a PP crystal cannot be reused for several different wavelengths, even if an hypothetical cavity length is modified to "select" a new frequency (see Chapter 4). For instance, the SHG bandwidth for a fundamental wavelength in the telecom band is as narrow as $1.3nm$ for a $10mm$ interaction length using high-intensity pulsed lasers [55, 56]. On the other hand, a birefringent crystal such as BBO or LBO uses birefringence phase matching, which can be continuously satisfied by simply adjusting the crystal's angle with respect to the incoming beam. This allows the same birefringent crystal to offer greater flexibility and be immediately reused for generating new frequencies by a straightforward mechanical angle adjustment after altering the cavity size and switching to a new fundamental wavelength. Indeed, even though recent studies have shown significant interest in expanding the phase matching bandwidth of Periodically Poled crystals in the telecommunication band [57, 58], BBO still provides enhanced bandwidth for shorter crystals [59].

Chapter 4

SHG Enhancement Cavity

As discussed in Chapter 3, continuous-wave SHG in a single pass through a nonlinear crystal typically yields low conversion efficiencies. To overcome this limitation, an optical resonator can be employed to enhance the power of the fundamental field travelling through the crystal. In a simple two-mirror cavity, it was found that repeated reflections drive the field toward a spatial distribution that does not vary from transit to transit (normal resonator mode) [60]. As a result, the profile of the field is reproduced at each round trip, and the power within the cavity can be significantly higher than the input power.

The next sections describe the main characteristics of a specific resonator type and show how it can be used to enhance the SHG process.

4.1 The Confocal Resonator

The confocal resonator consists of two identical spherical mirrors placed at a distance equal to their radius of curvature R. This results in an overlapping of their foci at the center of the resonator. The analytical treatment is given by Boyd and Gordon [61] and it is presented in a concise form proposed by [62]. The problem is treated under the scalar approximation, where the field is described as a scalar quantity U, as it is assumed to be nearly transverse and uniformly polarized.

4.1.1 Cavity Eigenfunctions and Resonant Frequencies

Considering a field distribution U corresponding to a cavity mode, it must reproduce itself when travelling from mirror 1 to mirror 2, separated by a distance L, apart from a constant amplitude and phase factor σ:

$$\sigma U(P_2) = \frac{-i}{2\lambda} \int_1 \frac{U(P_1) e^{ikr}(1+cos\theta)}{r} dS_1 \tag{4.1}$$

Here r is the distance between generic points $P_1(x_1, y_1)$ and $P_2(x_2, y_2)$ on the two mirrors, θ is the angle between the normal to the surface at point P_1 and the line connecting P_1 and P_2 and the integration is performed over the surface element dS_1 over P_1 (Figure 4.1).

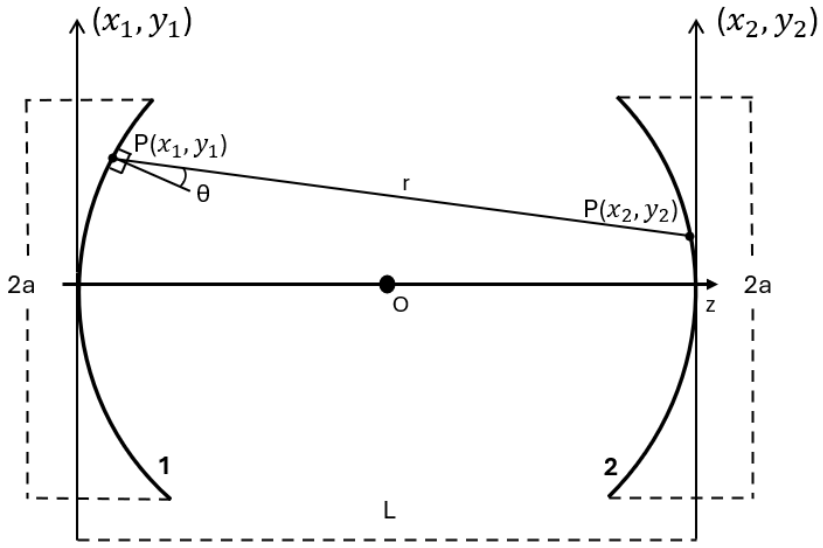

Fig. 4.1 Confocal configuration for a two-mirror optical resonator.

The constant σ can be expressed as $\sigma = |\sigma| e^{i\phi}$, where its absolute value gives the fractional power loss per pass due to diffraction ($\gamma_d = 1 - |\sigma|^2$), while 2ϕ represents the phase shift accumulated by the field in one round trip.

Equation 4.1 can be simplified if the lenght of the cavity is well above its transverse dimensions (mirror half-width a), as one can set $cos\theta \approx 1$ and $r \approx L$. To find a suitable approximation for the phase factor kr, the calculation of the distance

between P_1 and P_2 as a function of the coordinates of the two points is followed by an expansion in a Taylor series to give:

$$r \approx L - \frac{1}{L}(x_2 x_1 + y_2 y_1) + \varepsilon \tag{4.2}$$

This expression is a good approximation when the phase error ε is not significant compared to a full wave cycle. This condition holds if $N \ll \frac{L^2}{a^2}$, where $N = a^2/\lambda L$ is the Fresnel number of the cavity.

Introducing the dimensionless quantities

$$\xi = \sqrt{N}\frac{x}{a}, \quad \eta = \sqrt{N}\frac{y}{a}, \tag{4.3}$$

equation 4.1 finally reduces to a simplified, and dimensionless integral equation:

$$\sigma^* U(\xi_2, \eta_2) = -i \int_1 U(\xi_1, \eta_1) \exp\{i\pi[(\xi_1 - \xi_2)^2 + (\eta_1 - \eta_2)^2]\}\, d\xi_1 d\eta_1 \tag{4.4}$$

with $\sigma^* = \sigma\ exp(-ikL)$.

The problem can now be broken down into two independent one-dimensional integrals:

$$U(\xi, \eta) = U_\xi(\xi) U_\eta(\eta), \quad \sigma^* = \sigma_\xi^* \sigma_\eta^* \tag{4.5}$$

Looking for a separable solution, equation 4.4 gives:

$$\sigma_\xi^* U_\xi(\xi_2) = e^{-i\frac{\pi}{4}} \int_{-\sqrt{N}}^{\sqrt{N}} U_\xi(\xi_1) \exp(-i2\pi\xi_1\xi_2)\, d\xi_1 \tag{4.6}$$

$$\sigma_\eta^* U_\eta(\eta_2) = e^{-i\frac{\pi}{4}} \int_{-\sqrt{N}}^{\sqrt{N}} U_\eta(\eta_1) \exp(-i2\pi\eta_1\eta_2)\, d\eta_1 \tag{4.7}$$

The physical meaning of equation 4.6 is simple, as it describes the field distribution in a cavity made of two plane mirrors that are finite in the x direction (width 2a)

and effectively infinite in the y direction. Similar interpretation holds for equation 4.7.

The two-dimensional cavity mode is formed by the product of the two one-dimensional solutions. This combined solution is called a transverse electromagnetic mode, typically denoted as TEM_{ml} in laser physics, where m and l are integers indicating the mode orders in the x and y directions. At the same time, the overall eigenvalue for a TEM_{ml} mode is the product of the corresponding one-dimensional eigenvalues. This combined eigenvalue carries information about the total diffraction loss and phase shift of the TEM_{ml} mode:

$$U_{m,l} = U_{\xi,m}(\xi)U_{\eta,l}(\eta), \quad \sigma^*_{m,l} = \sigma^*_{\xi,m}\sigma^*_{\eta,l} \tag{4.8}$$

In the hypothesis of a high Fresnel number, the mirrors are either very large or very close together relative to the wavelength of the light. This minimizes diffraction effects, as the light has less opportunity to "spread out" and miss the mirror edges. If this assumption holds ($N \gg 1$), the solutions to equations 4.6 and 4.7 can be approximated by a product of a Gaussian function with a Hermite polynomial. Returning to original x and y coordinates, the eigenfunctions for the TEM_{ml} modes are given by:

$$U_{x,m}(x) = H_m\left[x\sqrt{\frac{2\pi}{L\lambda}}\right]\exp\left[-\frac{\pi x^2}{L\lambda}\right] \tag{4.9}$$

$$U_{y,l}(y) = H_l\left[y\sqrt{\frac{2\pi}{L\lambda}}\right]\exp\left[-\frac{\pi y^2}{L\lambda}\right] \tag{4.10}$$

where H_m and H_l are the Hermite polynomials of order m and l respectively. The overall field distribution for the TEM_{ml} mode is then:

$$U_{m,l}(x,y) = H_m H_l \exp\left[-\frac{\pi(x^2+y^2)}{L\lambda}\right] \tag{4.11}$$

For example, the fundamental mode TEM_{00} has a pure Gaussian distribution, following the field distribution of Figure 4.2 along both the x and y directions ($H_{m=0} = H_{l=0} = 1$). Experimentally, the intensity profile of such mode creates a circular luminous spot on an incident mirror.

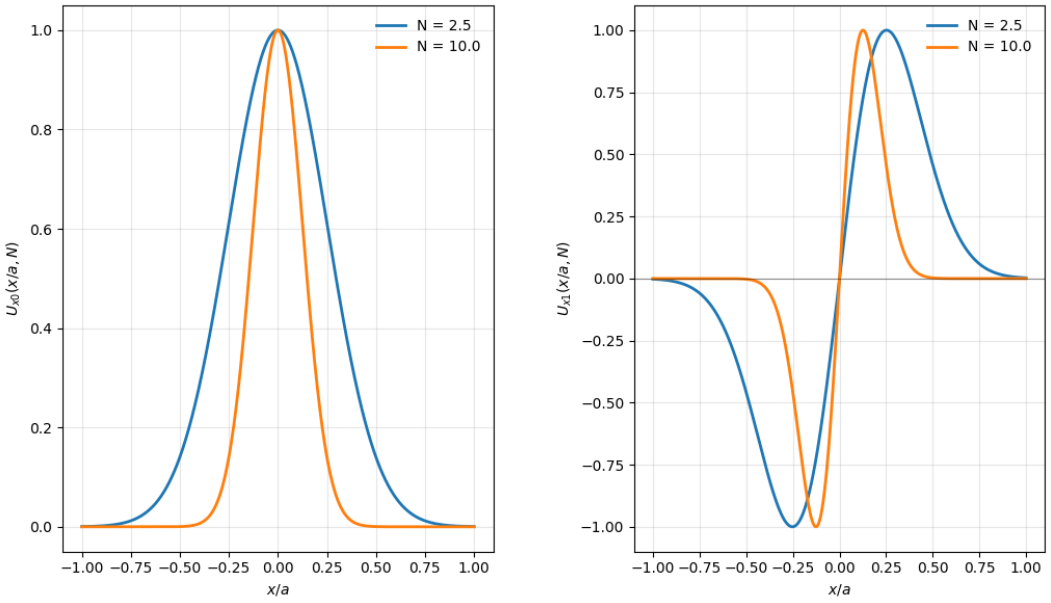

(a) (b)

Fig. 4.2 Normalized field distribution along dimension x with $H_m = 0$ (a) and $H_m = 1$ (b). The plots are presented for two different Fresnel numbers N and x is scaled with respect to the mirror half-width a.

On the other hand, higher-order modes, such as the TEM_{01}, will present a radial behaviour along the x direction as presented in Figure 4.2a, while Fig 4.2b shows the radial behaviour along the y direction.

The eigenvalues corresponding to the TEM_{ml} can be evaluated by dropping the limit imposed by the high Fresnel number approximation for a more meaningful description. The resonant frequencies are obtained by equating the phase of $\sigma^*_{m,l}$ to an integral number times π:

$$kL + \phi^*_{m,l} = n\pi \tag{4.12}$$

Equation 4.12 carries terms depending on λ ($\phi^*_{m,l}$ depends on the Fresnel Number too), therefore it allows for the calculation of the resonant frequencies as a function of the mode indexes. The resonant frequencies for a confocal resonator turns out to satisfy the relation:

$$\nu_{n,m,l} = \frac{c}{2L}\left(n + \frac{m+l+1}{2}\right) \tag{4.13}$$

where n is the longitudinal mode index, determining the number of half-wavelengths fitting inside the cavity of length L along the propagation direction z. The expression shows that modes having the same $2n+m+l$ values are degenerate, i.e., they resonate at the same frequency although having different spatial configurations. Moreover, the frequency spacing between adjacent longitudinal modes is the same as that of the simple Fabry-Perot resonator, given by $\Delta\nu = c/2L$. However, higher-order transverse modes are interspersed between the longitudinal modes if mode matching is not enforced. In fact, when it's the case, the spacing between adjacent resonant frequencies becomes $\Delta\nu = c/4L$, the Free Spectral Range (FSR) of the confocal resonator.

4.1.2 Cavity Mode Parameters and Gaussian Beams

Once the field distribution and resonant frequencies of the confocal resonator have been established, it can be shown that field distribution at any point inside (as well as outside) the resonator can be expressed as:

$$U_{m,l}(x,y,z) = \frac{w_0}{w(z)} H_m\left(\frac{\sqrt{2}x}{w(z)}\right) H_l\left(\frac{\sqrt{2}y}{w(z)}\right) \exp\left[-\frac{x^2+y^2}{w^2(z)}\right] \times \exp\left[-ikz - ik\frac{x^2+y^2}{2R(z)} + i(1+m+l)\phi(z)\right] \quad (4.14)$$

In 4.14, $w(z)$ is the beam radius at position z and w_0 is the beam waist, which is the measure of the beam size at the point of its focus. In the case of the confocal resonator:

$$w(z) = w_0\sqrt{1+\left(\frac{2z}{L}\right)^2} \quad (4.15)$$

where w_0 is located at the center of the resonator ($z = 0$) and it is given by:

$$w_0 = \sqrt{\frac{L\lambda}{2\pi}} \quad (4.16)$$

At the same time, the quantities $R(z)$ and $\phi(z)$ in the phase term of equation 4.14 are the radius of curvature of the wavefronts and the Gouy phase shift respectively:

$$R(z) = z + \frac{L^2}{2z}, \quad \phi(z) = \tan^{-1}\left(\frac{2z}{L}\right) \tag{4.17}$$

Note that for $z = 0$ (center of the resonator) we have $R = \infty$ and the wavefront is plane, while for $z = L/2$ (at the mirrors) $R = L$, matching the curvature of the mirrors.

In the general case, an ideal Gaussian beam can be represented as the fundamental transverse mode TEM_{00} of the Hermite-Gaussian orthonormal mode basis, fully specified by its waist w_0 and Rayleigh range z_R. In this case, equation 4.15 and equation 4.17 are written as the standard Gaussian-beam relations:

$$w(z) = w_0\sqrt{1+\left(\frac{z}{z_R}\right)^2}, \quad R(z) = z + \frac{z_R^2}{z}, \quad \phi(z) = \tan^{-1}\left(\frac{z}{z_R}\right) \tag{4.18}$$

where the Rayleigh range z_R is related to the waist w_0 by $z_R = \frac{\pi w_0^2}{\lambda}$.

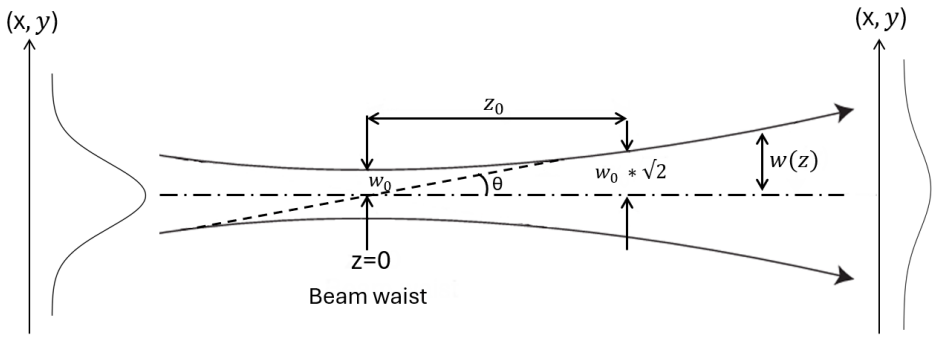

Fig. 4.3 Variation of spot size $w(z)$ of a Gaussian Beam.

The Rayleigh range is a measure of the length of the waist region, representing the axial distance over which the beam radius increases by a factor $\sqrt{2}$ (Figure 4.3).

Specializing these general relations to the symmetric confocal resonator scenario shows that $z_R = \frac{L}{2}$, meaning $z_R = R$ for the resonant mode.

4.1.3 Mode Matching and *ABCD* Matrix Formalism

To efficiently couple light into a resonator, the spatial profile of the incoming beam must closely match the spatial profile of one of the cavity's eigenmodes. This process, known as mode matching, is a fundamental step toward maximizing power buildup in the cavity. In particular, for a confocal resonator, the incoming beam must have a waist w_0 located at the cavity center and given by equation 4.16.

To achieve mode matching, if the incoming beam is Gaussian, it can be focused to the desired waist using a focal lens placed at an appropriate distance from the cavity. The transformation of the beam parameters through the lens can be analyzed using the ABCD matrix formalism [41]. In this framework, a Gaussian beam is described by the complex beam parameter $q(z)$, defined as

$$q(z) = z + iz_R, \tag{4.19}$$

whose reciprocal encodes the wavefront curvature $R(z)$ and spot size $w(z)$:

$$\frac{1}{q(z)} = \frac{1}{R(z)} - i\frac{\lambda}{\pi n w^2(z)}. \tag{4.20}$$

Propagation through a first-order optical system with ray-transfer matrix $\begin{pmatrix} A & B \\ C & D \end{pmatrix}$ is then written compactly via the ABCD law

$$q_2 = \frac{Aq_1 + B}{Cq_1 + D}. \tag{4.21}$$

The ray matrix for the optical system consisting of a thin lens of focal length f followed by a straight section of propagation of length d is [63]:

$$\begin{pmatrix} 1 - \frac{d}{f} & d \\ -\frac{1}{f} & 1 \end{pmatrix} \tag{4.22}$$

If a gaussian beam is incident on the lens placed at its waist (Figure 4.4), the input beam parameter is $q = iz_R$ and $R = \infty$.

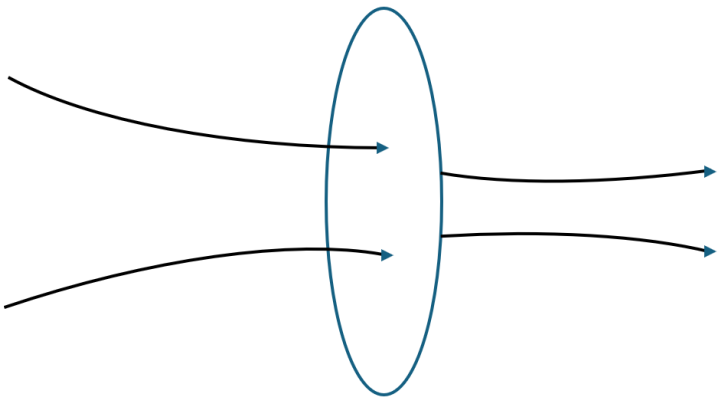

Fig. 4.4 A Gaussian beam incident on a lens at its waist is focused to a new waist.

Applying the matrix tranformation, the output beam parameter is:

$$q_2 = \frac{-(i\pi\omega_0^2/\lambda)(1-d/f)+d}{(i\pi\omega_0^2/\lambda f)+1} \tag{4.23}$$

Equating imaginary and real part of q_2 to equation 4.20, the dependence of the output waist and radius of curvature on their poisition behind the lens d can be found:

$$w_2(d) = w_0^2\left(1-\frac{d}{f}\right)^2 + w_0^2\left(\frac{d}{z_R}\right)^2 \tag{4.24}$$

and

$$R_2(d) = \frac{(d/z_R)^2+(1-d/f)^2}{d/z_R^2-(1/f)(1-d/f)}, \tag{4.25}$$

To find the location of the new waist w_2 after the lens, one can set the denominator of $R_2(d)$ to zero, obtaining:

$$d = \frac{f}{1+(f/z_R)^2}, \tag{4.26}$$

representing the distance from the lens to the new waist.

Substituting this value of d back into the expression for $w_2(d)$, the size of the new waist is found to be:

$$w_0' = \frac{\lambda f}{\pi w_0} \frac{1}{\sqrt{1+(f/z_R)^2}} \approx \frac{\lambda f}{\pi w_0} \quad \text{for } f \ll z_R. \tag{4.27}$$

By choosing the focal length f and the initial waist w_0 appropriately, it is possible to achieve the desired waist w_0' at the cavity center, enabling efficient mode matching into the resonator.

4.1.4 Cavity Power Enhancement

When a resonator is driven by an external laser source, the circulating power inside the cavity can be significantly higher than the input power. To quantify this enhancement, we again consider the SHG theory presented in Chapter 3, but we rewrite equation 3.36 as a function of the single-pass conversion efficiency, expressed in the International System of Units (SI) as [64, 65]:

$$E_{nl} = \frac{16\pi^2 d_{eff}^2 L}{\varepsilon_0 c \lambda_1^3 n_2 n_1} e^{-\alpha_{eff} L} h_m(B,\xi), \tag{4.28}$$

where all the presented quantities are already described in Section 3.4. The single-pass output power at the second harmonic frequency ω_2 is then:

$$P_{2\omega} = E_{nl} P_\omega^2. \tag{4.29}$$

Introducing the optical cavity, the circulating power at the fundamental frequency ω depends on the input power P_{in} as [66]:

$$P_{c,\omega} = \frac{T_1 P_{in}}{\left[1-\sqrt{(1-T_1)(1-l_{cav})(1-E_{nl}P_{c,\omega})}\right]^2} P_{in}, \tag{4.30}$$

where T_1 is the transmission of the input coupler mirror and l_{cav} is the round-trip linear intracavity loss factor. Here we are assuming a perfect mode matching between the input beam and the cavity mode (see Section 4.1.3), otherwise a mode matching

efficiency η should be included as a multiplicative factor to P_{in}. The SHG power is finally

$$P_{2\omega} = E_{nl} P_{c,\omega}^2. \tag{4.31}$$

From equation 4.30 it is possible to maximize the circulating power by choosing the optimal input coupler transmission T_1:

$$T_{opt} = \frac{l_{cav}}{2} + \sqrt{\frac{l_{cav}^2}{4} + E_{nl} P_{in}}. \tag{4.32}$$

This occurs when the input coupler transmission matches the total round-trip loss inside the cavity and such condition is known as impedance matching.

4.2 Our Cavity

The second-harmonic process investigated in this work is realized using a BBO crystal. In the adopted configuration, illustrated in Figure 4.5, two incoming photons polarized along the ordinary axis are converted into a single photon at twice the frequency, polarized along the extraordinary axis. According to the vendor, the crystal must be tilted around the y-axis so the incoming light hits the crystal's optical axis at about a 20° angle to get the best phase matching. As explained in Section 3.3, this setup corresponds to a collinear type-I phase-matching geometry for second-harmonic generation.

As highlighted in Section 3.5, BBO is a very attractive nonlinear medium for second-harmonic generation over a broad wavelength range. However, its effective nonlinear coefficient is relatively small in continuous-wave operation: from Figure 3.4 it is evident that, even when the focusing parameter ξ is optimized to its ideal range between 1.39 and 2.84, the maximum single-pass second-harmonic power remains at the level of a few microwatts for input powers on the order of watts. Consequently, to obtain a practically useful SHG output, it is necessary to increase the circulating fundamental power inside the crystal by placing it in an enhancement cavity.

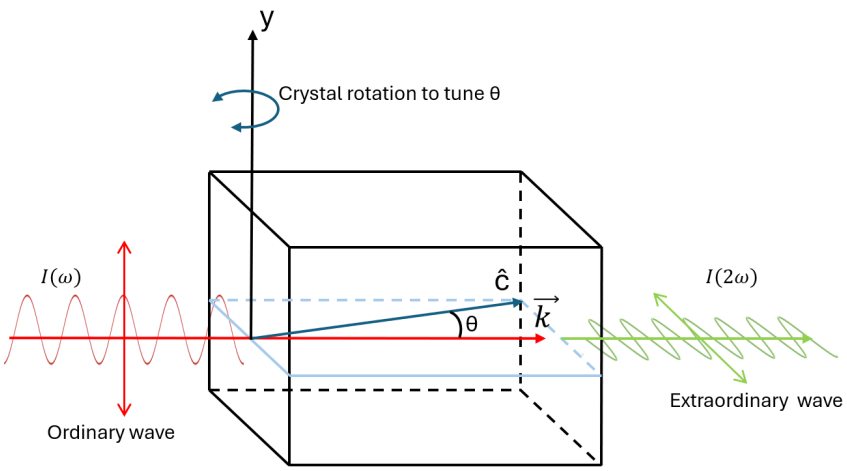

Fig. 4.5 Our Type I phase matching configuration for SHG in BBO crystal.

4.2.1 Cavity Design

The confocal resonator introduced in Section 4.1 is a natural choice for our purposes, since it offers a simple and robust architecture that is relatively easy to align and maintain stable operation.

4.2.1.1 Intra-Cavity Losses

A first key parameter in the design is the round-trip intra-cavity loss factor, l_{cav}. This quantity has a dramatic impact on the second-harmonic generation efficiency. The effect of losses is illustrated in Figure 4.6, where the second-harmonic output power is shown as a function of the intra-cavity loss for different single-pass conversion efficiencies.

The conversion efficiencies used in Figure 4.6 correspond to the optimal values for each BBO crystal length shown in Figure 3.4 (5, 10, and 15 mm). These values were chosen to maximize the single-pass second-harmonic power for an input power of 2W. As the figure clearly shows, even modest linear losses strongly degrade the SHG output. When losses exceed about 2.5%, the output power drops to just a few milliwatts, making efficient conversion almost impossible.

To reduce these losses, the BBO crystal was coated with high-quality anti-reflection (AR) coatings at the fundamental wavelength. These coatings achieve a

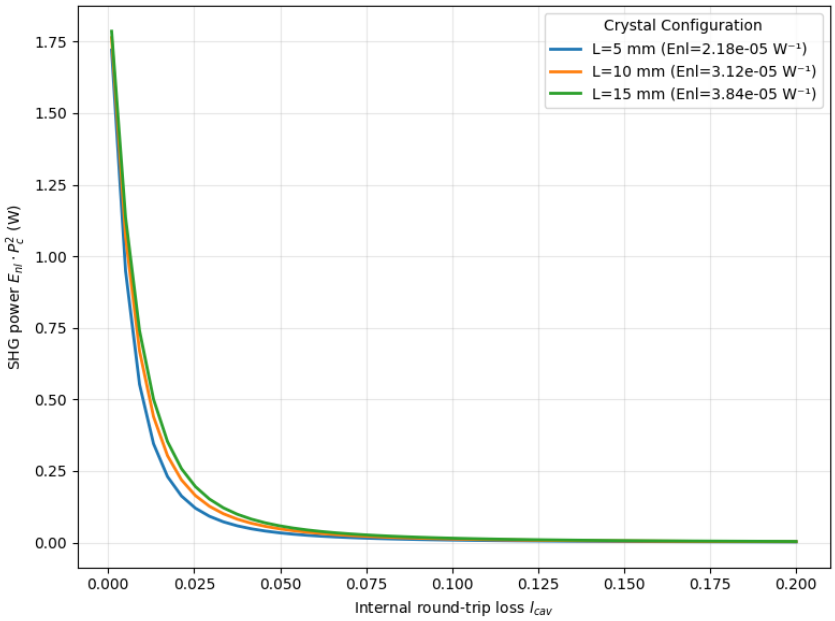

Fig. 4.6 Second harmonic output power as a function of the intra-cavity loss factor for different single-pass conversion efficiencies and an input power of $P_{in} = 2W$.

residual reflectivity of $R_{res} < 0.2\%$ per surface, minimizing unwanted reflections that would otherwise contribute significantly to the total cavity loss.

The total linear losses inside the cavity can be approximated by considering all the main loss mechanisms:

$$l_{cav} \approx 4R_{res} + (1 - R_{mirr}) + 2(1 - e^{-\alpha L}). \tag{4.33}$$

Here, R_{mirr} is the reflectivity of the output coupler mirror at the fundamental wavelength, and α is the bulk absorption coefficient of the crystal. The first term accounts for the residual reflections from the two crystal surfaces (four interfaces in a round trip). The second term represents the fundamental power lost through transmission at the output coupler. The third term accounts for absorption within the crystal material over its length L.

To minimize losses through the output coupler, the output mirror reflectivity was chosen to be $R_{mirr} \geq 99.95\%$ at the fundamental wavelength. This choice sets an upper bound on the achievable intra-cavity losses of roughly 0.99% if we consider a crystal length of 15mm and an absorption coefficient $\alpha \leq 0.05\text{cm}^{-1}$ (as specified by the crystal vendor). Note that the input-coupler reflectivity is not included explicitly

in l_{cav}, since it is instead treated within the impedance-matching condition. From equation 4.32, the optimal input coupler transmission is found to be approximately $T_1 \approx 1.35\%$, which ensures maximum power coupling into the cavity mode.

4.2.1.2 Crystal and Cavity Length Selection

The analysis presented in Section 3.5 provides additional constraints on both the crystal length and the cavity geometry. In general, longer crystals yield higher conversion efficiency due to the increased interaction length. However, the crystal length also determines the optimal Boyd–Kleinman focusing parameter ξ for a given beam waist inside the crystal.

For a crystal length of $L = 15$mm, the analysis in Figure 3.4a indicates that the optimal beam waist at the cavity center should be approximately $w_0 \approx 51\mu$m. Using equation 4.16 for the waist of a confocal resonator, achieving such a small waist would require a cavity length of only about 10mm. This poses a practical problem: the cavity would be shorter than the crystal itself, making the design physically impossible.

A more practical compromise was therefore adopted. We selected mirrors with a radius of curvature $R = 2.5$cm, leading to a stable confocal cavity of length $L = 5$cm. This cavity length yields a beam waist of $w_0 \approx 111\mu$m at its center, which is larger than the ideal value but still provides acceptable focusing characteristics.

Table 4.1 summarizes the main parameters of the designed cavity, including both the geometric and optical characteristics.

Parameter	**Value**
Cavity Length L	5 cm
Mirror Focal Length f	2.5 cm
Crystal Length $L_{crystal}$	15 mm
Double Refraction Parameter B	7.13
Beam Waist w_0	111 μm
Focusing Parameter ξ	0.30
Estimated Intra-Cavity Losses l_{cav}	0.99%
Input Coupler Transmission T_1	1.35%

Table 4.1 Main parameters of the designed confocal resonator for SHG in BBO crystal.

4.2.1.3 Expected Performance

Setting the crystal and the cavity lengths, we can evaluate the Boyd–Kleinman function and estimate the expected conversion efficiency. In our setup, the focusing parameter is $\xi \approx 0.30$, which is below the optimal range identified in Section 3.5. This means the beam isn't as tightly focused as needed for the best conversion efficiency.

The double refraction parameter is found to be $B \approx 7.13$. Using the analytical approximation provided in [67], the associated value of the Boyd–Kleinman function is $h_m \approx 0.06$. Although this is well below the theoretical maximum, the strong power boost from the resonant cavity should compensate for the less-than-ideal focusing.

Figure 4.7 shows the expected second-harmonic output power and conversion efficiency as a function of the input power, based on the analytical model of equations 4.30 and 4.31. With an erbium-doped fiber amplifier, the emitted light at the fundamental wavelength can reach powers up to a few watts. For an input power of $P_{\text{in}} = 2$ W, we estimate a maximum second-harmonic output power of approximately $P_{2\omega} \approx 530$ mW, corresponding to a conversion efficiency of about 26.5%. While this represents a best-case scenario, assuming ideal alignment and minimal additional losses, it provides an initial target for the experimental implementation.

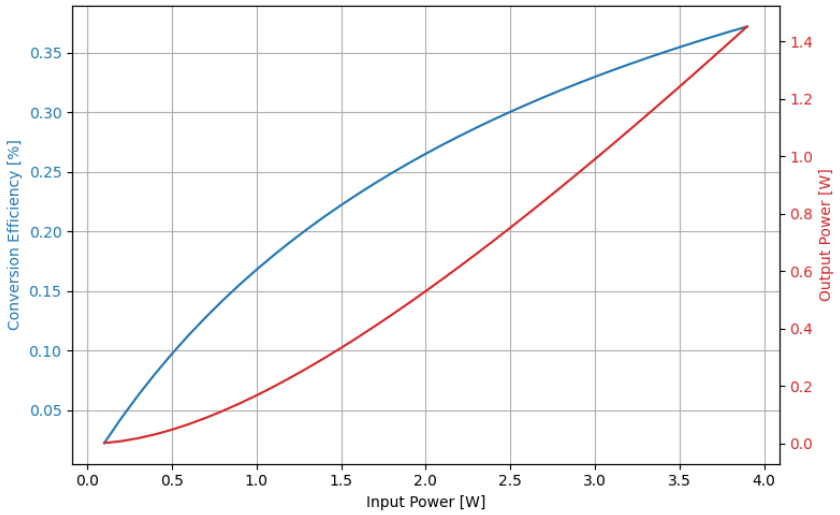

Fig. 4.7 Predicted second-harmonic output power (red) and conversion efficiency (blue) as a function of the input power at 1556 nm, based on the analytical model.

To validate this analytical prediction, numerical simulations were performed using the SNLO software package, which uses a propagation model that explicitly accounts for spatial beam profiles, crystal birefringence, walk-off, and the detailed interaction between the fundamental and second-harmonic fields as they build up over multiple round trips.

The first step was to calculate the cavity mode properties using SNLO's *Cavity* function. Table 4.2 shows the beam parameters predicted for our confocal cavity design.

Table 4.2 SNLO cavity mode parameters for the linear confocal resonator.

Parameter	**Value**
Rayleigh range in crystal	40.5 mm
Beam waist in crystal ($1/e^2$ radius)	110.90 μm
Beam waist in crystal (FWHM)	130.57 μm
Beam size at mirror ($1/e^2$ radius)	148.46 μm
Beam size at mirror (FWHM)	174.80 μm

Cavity mode calculations confirm that the beam radius at the cavity center is approximately $w_0 \approx 111$ μm, which is in excellent agreement with the analytical estimate in equation 4.16. The Rayleigh length is approximately 40.5 mm, much larger than the crystal length of 15 mm. This ensures good collimation of the beam throughout the interaction region and validates our assumption about a constant beam radius within the crystal.

Using these cavity mode parameters and the design parameters from the previous section (crystal length, surface reflectivity, and crystal volume absorption coefficient), we simulated the frequency doubling process within the cavity using the *2D-cav-LP* function. At a wavelength of 1556 nm and an input power $P_{\text{in}} = 2.0$ W, the simulation results predict that the frequency doubling output power stabilizes at a wavelength of 778 nm after a brief transient phase, approximately $P_{2\omega} \approx 650$ mW. As shown in Figure 4.8, this corresponds to a conversion efficiency of approximately 32.5%.

The simulation also indicates a residual fundamental leakage of approximately a few milliwatts through the output coupler, confirming that the cavity is operating near the impedance-matched condition for optimal power coupling.

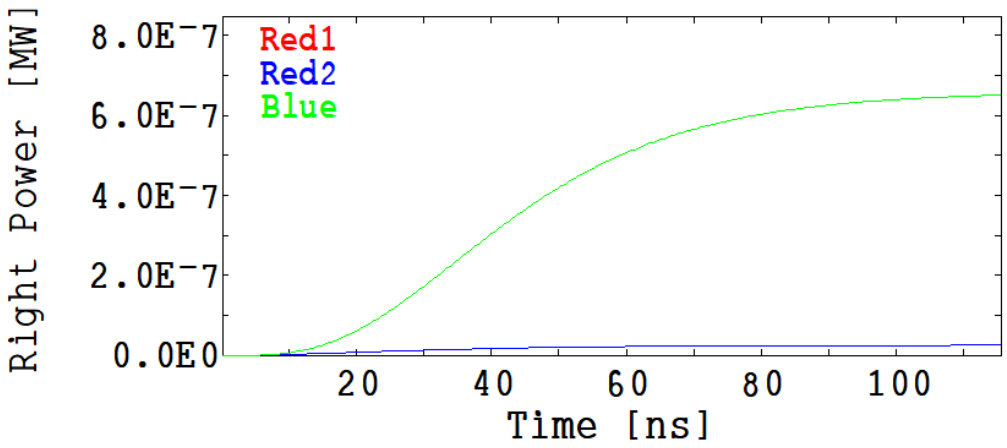

Fig. 4.8 Image generated from the SNLO simulation of the second-harmonic output power ("Blue" label) of the confocal cavity as a function of time for an input power of $P_{\text{in}} = 2$ W at 1556 nm. After an initial build-up phase, the SHG power stabilizes at approximately 650 mW.

The SNLO simulation predicts a conversion efficiency which is in good agreement with the analytical Boyd-Kleinman model prediction of 26.5%. The similarity between these two independent approaches is encouraging and provides confidence in the cavity design, always remembering that they assume ideal conditions, such as perfect alignments and optimal phase matching. In practice, real experimental implementations could experience additional loss mechanisms and alignment imperfections.

In any case, both models predict output powers in the range of 500-650 mW at 778 nm for a 2 W input, which are more than sufficient for our atomic spectroscopy application, where typical powers of 10-20 mW are adequate to interrogate the Rb-87 two-photon transition while avoiding saturation and AC Stark shifts. Moreover, these results align well with experimental results reported in the literature for similar cavity-enhanced SHG setups [65, 68–70]

Chapter 5

Clock Experimental Realization

Two-photon optical clocks based on rubidium atoms have been previously investigated and several experimental realizations have been demonstrated over the years [71–73]. As discussed in Section 2.2.6, two-photon transitions are especially attractive because they enable Doppler-free spectroscopy when the atomic vapor is interrogated with two counter-propagating laser beams. Moreover, two-photon excitation is often monitored via fluorescence at a distinct wavelength from that of the probe laser. This, combined with the large number of atoms in a vapor cell, results in clock transition measurements with excellent signal-to-noise ratio without needing complex laser cooling or trapping systems. This intrinsic simplicity makes two-photon optical clocks well suited for compact designs, also opening the door to further miniaturization through photonic integrated circuit (PIC) implementations [74].

In the context of this work, an important practical feature is that the 778.1 nm light required for driving the transition can be conveniently produced by second harmonic generation from the 1556.2 nm radiation. As a consequence, it's possible to exploit mature laser sources in the telecommunications C-band, together with erbium-doped technology.

Published demonstrations of two-photon optical clocks based on rubidium atoms have reported strong stability performance, with long-term fractional frequency stability on the order of 5×10^{-15} when averaged over multi-day timescales [75], and short-term stability near 1.5×10^{-13} at an averaging time of 1 s [76]. However, for averaging times from the medium to long term, the achieved performance is often

limited by systematic fluctuations. In particular, variations of the AC Stark (light) shift caused by probe-laser power fluctuations, together with instabilities of the vapor-cell temperature, are commonly identified as dominant contributors [77, 78].

5.1 Spectroscopy Characterization

In ^{87}Rb specifically, the key transitions, depicted in Figure 5.1 [79], connect the ground state $5S_{1/2}$ to the excited $5D_{5/2}$ state. Among them, the two-photon transition at 778.1nm is the one addressed in our experiment. The excited state then undergoes a cascade decay through the intermediate $6P_{3/2}$ level, finally returning to the ground $5S_{1/2}$ state while emitting blue fluorescence at 420 nm. The 420 nm clock signal indeed originates from the cascade $5D_{5/2} \rightarrow 6P_{3/2} \rightarrow 5S_{1/2}$, and unwanted near-infrared light is prevented from being detected by using standard optical filters.

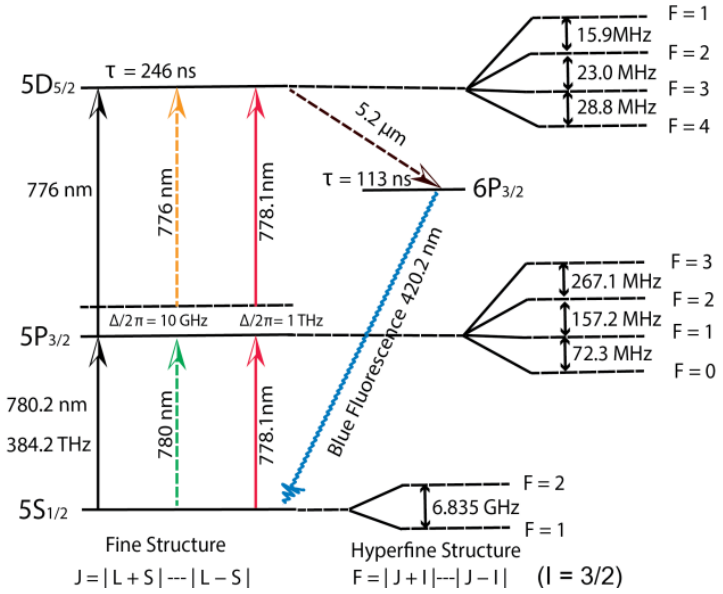

Fig. 5.1 Key transitions in the rubidium two-photon optical clock. Figure adapted from Obaze-Adeleke, A. C., Semon, B., and Bandi, T. N., *Photonics* **12**(5), 513 (2025). Open Access.

5.1.1 Experimental Setup

To study the two-photon transition, we used a preliminary experimental setup (see Figure 5.2). The 778nm radiation emitted by an ECDL probe laser is collimated into the free-space apparatus, with the collimator setting the beam radius to approximately 0.49mm. Downstream of the collimator, a half-wave plate (HWP) and a polarizing beam splitter (PBS) are used to control and monitor the laser power incident on a rubidium vapor cell. The vapor cell is 75mm long and contains ^{87}Rb and ^{85}Rb vapors, whose densities are temperature-controlled by a dual-channel resistance-heating controller. The laser beam is focused into the cell using a convex lens (L1) of focal length $f = 125$mm to increase the power intensity within the interaction region and thus enhance the two-photon transition probability. The beam is finally retro-reflected using a concave mirror of focal length $f = 75$mm to realize the counter-propagating geometry necessary for Doppler-free excitation. Of fundamental importance is the quarter-wave plate (QWP) placed before the cell, which converts the linear polarization of the incoming (and reflected) beam into circular polarization, with an effect of enhancing the two-photon transition rate [80]. The reflected beam is further deviated by the QWP and PBS combination to prevent back reflections from entering the laser cavity.

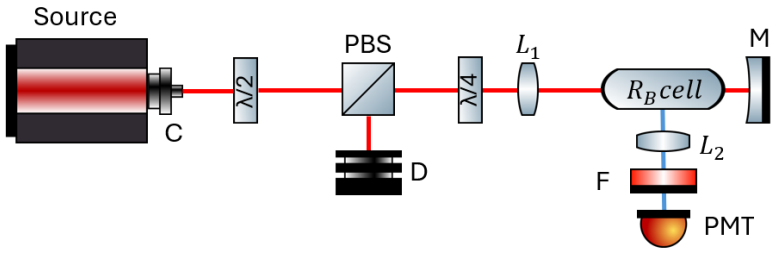

Fig. 5.2 Schematic of the experimental setup for two-photon spectroscopy of rubidium atoms. C: Fiber Collimator; $\lambda/2$: Half-Wave Plate; PBS: Polarizing Beam Splitter; D: Beam Dump; $\lambda/4$: Quarter-Wave Plate; L1, L2: Lenses; M: Mirror; F: Optical Filter; PMT: Photomultiplier Tube. Red lines indicate the 778 nm probe laser beam, while blue lines represent the 420 nm fluorescence.

With the excitation of the two-photon transition occurring within the vapor cell, the emitted blue fluorescence at 420 nm is collected using a bi-convex lens (L2) of

focal length $f = 25$mm and directed onto a photomultiplier tube (PMT) for detection. An optical filter (F) is placed in front of the PMT to block any residual infrared light coming from the probe laser.

5.1.2 Spectroscopy Results

5.1.2.1 Ground and Excited Hyperfine Spectrum

Using the setup described above, we performed spectroscopy of the $5S_{1/2} \rightarrow 5D_{5/2}$ two-photon transition in ^{87}Rb. The laser frequency is scanned across the two-photon resonance by applying a voltage ramp to the source piezoelectric transducer (PZT). In this way, we recorded the fluorescence signal as a function of the laser frequency as a few GHz were inspected around the resonance. By feeding the PMT output to a digital oscilloscope, we were able to visualize the fluorescence in terms of the applied PZT voltage as a function of time. Assuming the PZT voltage is approximately linear with the laser frequency response, the reconstruction of the two-photon spectrum was possible by calibrating the time axis into frequency units using a calibration factor $c = \frac{\Delta_f}{\Delta_t}$. Δ_f represents a known frequency interval identified from two spectral features separated by the corresponding measured time Δ_t on the oscilloscope. As for the frequency interval, we considered the well known hyperfine spacing between the $F = 1$ and $F = 2$ ground states of ^{87}Rb, reported in section 2.2.4 (independent of their relative position along the voltage ramp). In particular, addressing a two-photon transition, a change in laser frequency Δ_f corresponds to a change $2\Delta_f$ in terms of two-photon excitation energy. Therefore, once the corresponding time interval Δt between the two features in the fluorescence signal is known, the frequency-time calibration factor was obtained considering half of the $F = 1$ and $F = 2$ rubidium ground states distance. By multiplying the time axis by c, we thus reconstructed the two-photon spectrum in frequency units, as shown in Figure 5.3.

The laser power incident on the vapor cell during this measurement and the cell temperature are parameters that were adjusted according to the results obtained in Figures 5.5 and 5.6. In particular, the cell temperature was set to $T \approx 90^{\circ}C$ and the laser power to $P = 25$mW.

Figure 5.3 shows the main detected peaks while increasing laser frequency according to the piezo scan. The two large peaks at the center of the plot correspond

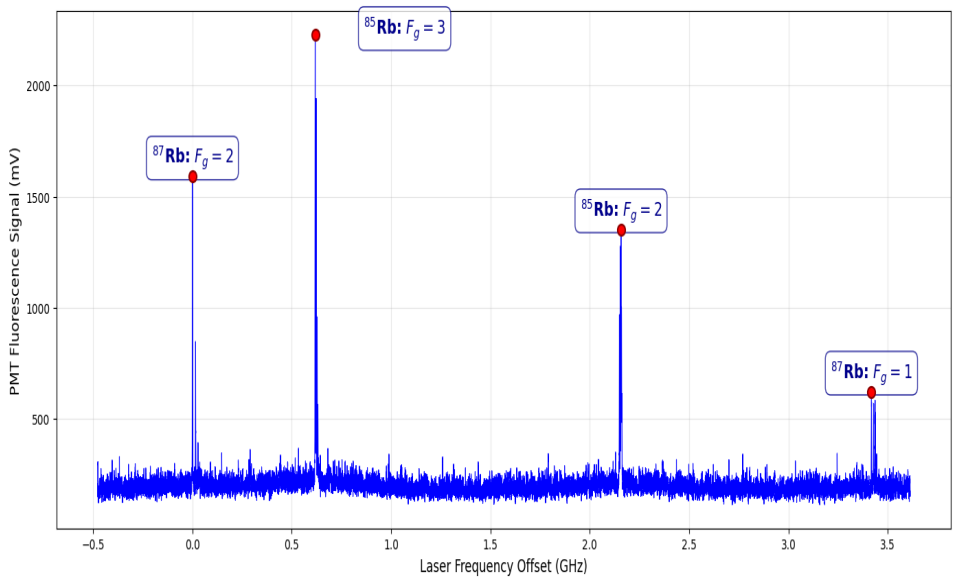

Fig. 5.3 Two-photon spectrum of the $5S_{1/2} \rightarrow 5D_{5/2}$ transition in ^{87}Rb, recorded via the 420 nm fluorescence as a function of the laser frequency. The frequency axis was calibrated using the known hyperfine splitting between the $F = 1$ and $F = 2$ ground states.

to the two-photon transitions from the third and second hyperfine ground state levels ($F_g = 3$ and $F_g = 2$, respectively) to the excited $5D_{5/2}$ state of ^{85}Rb. The leftmost and rightmost peaks correspond instead to the two-photon transitions from the two hyperfine ground state levels ($F_g = 2$ and $F_g = 1$, respectively) to the excited $5D_{5/2}$ state of ^{87}Rb.

Our work focuses on the leftmost (i.e. lowest-frequency) two-photon transition of ^{87}Rb. After identifying this feature, we reduced the scan range and acquired a higher-resolution spectrum around the resonance. The goal of this measurement is to address the transition originating from the ground hyperfine level $F_g = 2$ and to scan the laser frequency only in the immediate vicinity of the resonance, in order to resolve the hyperfine structure of the excited $5D_{5/2}$ state more clearly. The resulting spectrum is reported in Figure 5.4.

The oscilloscope records the PMT signal as a function of time, therefore another calibration step is required to convert the horizontal axis into frequency units. Here, the time-to-frequency conversion was obtained by using half of the known hyperfine splitting between the $F_e = 4$ and $F_e = 3$ levels of the excited $5D_{5/2}$ state, reported in Figure 5.1.

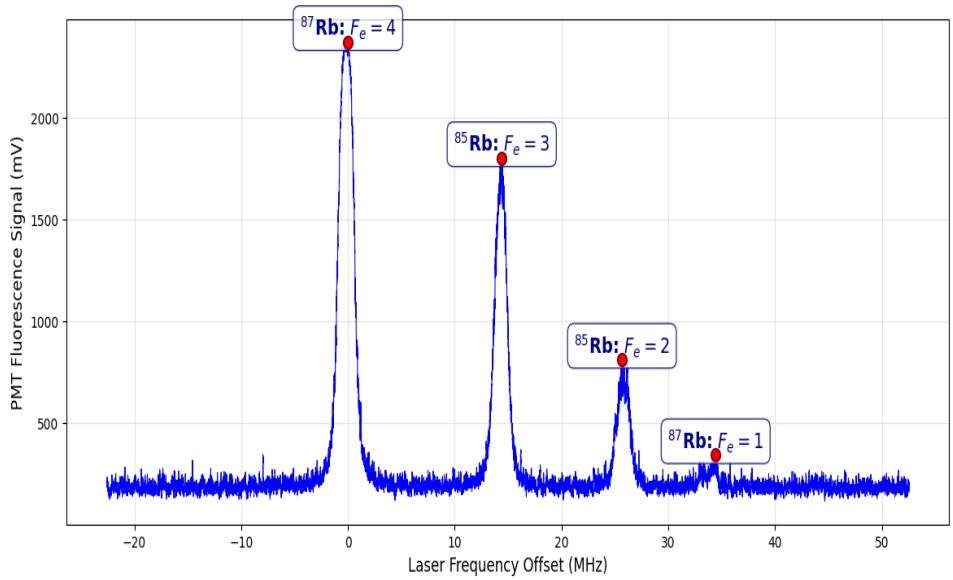

Fig. 5.4 High-resolution two-photon spectrum of the $5S_{1/2}(F_g = 2) \rightarrow 5D_{5/2}$ transition in ^{87}Rb, highlighting the excited state hyperfine structure.

As shown in Figure 5.4, the main spectroscopic features are well resolved and can be clearly identified. The relatively large separation between these peaks is one of the reasons why the ^{87}Rb two-photon transition is often preferred over the stronger ^{85}Rb two-photon transition, which typically exhibits lines that are closer together. In practice, a reduced spectral separation makes the lock point more susceptible to systematic drifts and experimental variations (e.g. cell temperature, optical power, and beam alignment), even when the detected fluorescence signal is larger.

5.1.2.2 Power and Temperature Dependence of the Two-Photon Signal

Before locking the laser frequency to the two-photon transition, it's fundamental to optimize the operating conditions for maximum signal strength and stability. For this reason, we investigated the dependence of the detected fluorescence signal on the laser power and the vapor cell temperature.

The spectroscopic signal of the $F_g = 2 \rightarrow F_e = 4$ two-photon transition of ^{87}Rb was recorded while varying the laser power incident on the vapor cell from 7mW to 40mW, for two fixed cell temperatures of $80°C$ and $90°C$. For each laser power value, the fluorescence signal amplitude and FWHM were recorded several times

and the average peak value was computed to improve measurement accuracy. The results are reported in Figure 5.5.

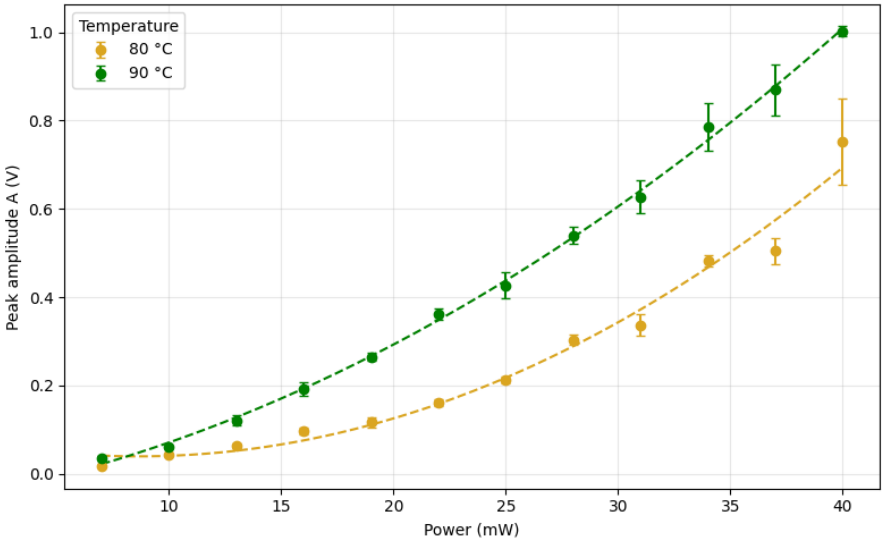

(a)

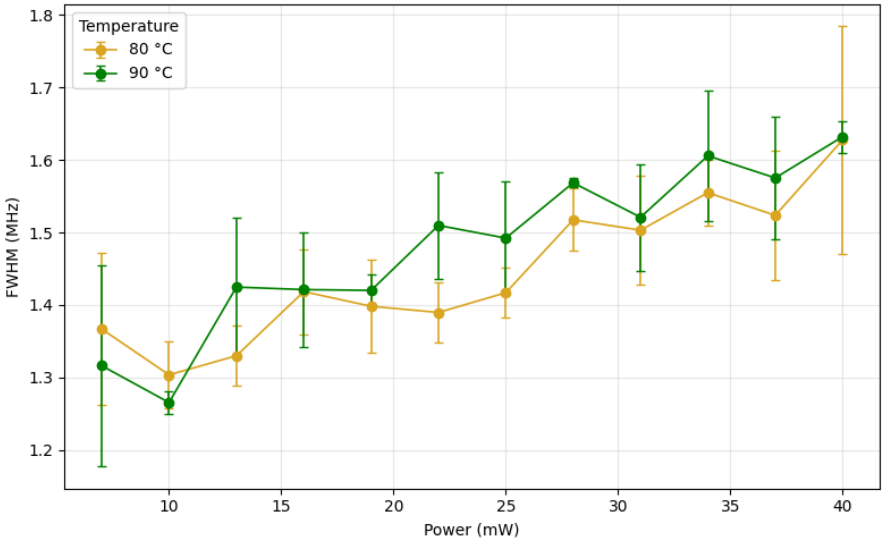

(b)

Fig. 5.5 (a) Fluorescence signal amplitude and (b) FWHM of the $F_g = 2 \rightarrow F_e = 4$ two-photon transition of ^{87}Rb as a function of the laser power incident on the vapor cell, for two fixed cell temperatures of $80°C$ and $90°C$.

The fluorescence signal amplitude shows a clear increasing trend as the optical power is raised. In particular, the dependence follows the quadratic law predicted by equation 2.13 and is consistent with previous experimental observations [72]. At

the same time, large optical powers lead to a slight increase in the spectroscopic linewidth, indicating a small but measurable power broadening. As for the measurements regarding the FWHM, the values lie in the range $1.2 - 1.6MHz$, above the two-photon transition natural linewidth of $330kHz$. This excess can be attributed to imperfect laser stabilization and finite intrinsic linewidth, as well as to small optical misalignments present in this initial clock design.

Similarly, increasing the cell temperature, larger fluorescence signals are detected due to the increased atomic density within the vapor cell. The result was further confirmed by keeping the laser power fixed at 40mW and recording the fluorescence signal as a function of the cell temperature. In particular, the temperature was varied from $65°C$ to approximately $90°C$ (the maximum allowed by the heater controller), and the results, showing a linear dependence between peak amplitude and temperature, are reported in Figure 5.6. Within this temperature range, instead, no substantial variations in the peak linewidth were recorded.

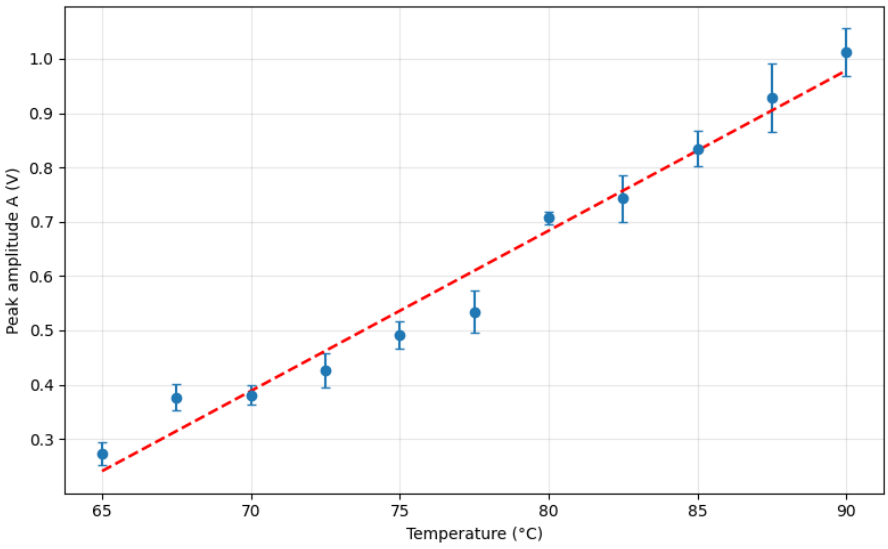

Fig. 5.6 Fluorescence signal amplitude of the $F_g = 2 \rightarrow F_e = 4$ two-photon transition of ^{87}Rb as a function of the vapor cell temperature, for a fixed laser power of 14mW.

Increasing both the laser power and the cell temperature results in a stronger spectroscopic signal because we are still below the saturation point, where the signal would level off. Although this improves the signal-to-noise ratio, it also causes a wider FHWM. This leads to a weaker locking error signal, which reduces the feedback loop's effectiveness in suppressing laser shifts (see next Section). For the next laser frequency stabilization experiment, we will operate at the maximum cell

temperature of 90 degrees and keep the optical power around 25 mW. This offers a good balance between a strong spectroscopic signal and a narrower transition linewidth.

5.2 Locking to the Two-Photon Transition

Once the two-photon transition of interest was identified and the operating conditions were optimized, we proceeded to lock the laser frequency to the center of the $F_g = 2 \rightarrow F_e = 4$ resonance. The objective is to produce an error signal that can be fed back to the laser piezo in order to stabilize its frequency to the atomic transition. For this purpose, we employed the frequency modulation spectroscopy technique with lock-in electronics, imposing a dither on the laser frequency and demodulating the fluorescence signal at the same frequency to obtain a dispersive error signal.

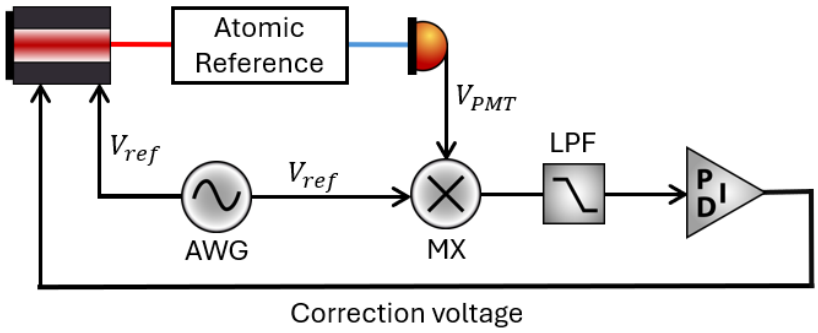

Fig. 5.7 Schematic of the experimental setup for laser frequency stabilization to the two-photon transition in ^{87}Rb. The additional components with respect to Figure 5.2 are AWG: Arbitrary Waveform Generator; MX: Mixer; LPF: Low-Pass Filter; PID: Proportional-Integral-Derivative Controller.

When we dither the laser frequency at ω_d, the transmitted light intensity oscillates as the laser sweeps repeatedly across the absorption line. The PMT converts this oscillating optical intensity into an oscillating voltage signal with a certain frequency ω:

$$V_{PMT} = A\sin(\omega t + \phi), \tag{5.1}$$

supposing the amplitude A doesn't vary significantly during the dither cycle. This signal is fed into a RF frequency mixer, which multiplies it by a reference signal at the dither frequency ω_d:

$$V_{ref} = B\sin(\omega_d t). \tag{5.2}$$

Assuming that these signals have been made in phase, the mixer multiplies these two signals together, producing an output that contains components at the sum and difference frequencies:

$$V_{mixer} = V_{PMT} \cdot V_{ref} = \frac{AB}{2}\left[\cos(\omega t - \omega_d t) - \cos(\omega t + \omega_d t)\right]. \tag{5.3}$$

The frequency ω of the PMT signal oscillation, as well as the error signal generated through a low pass filter after the mixer, depends on the laser's position relative to the atomic resonance (Figure 5.8).

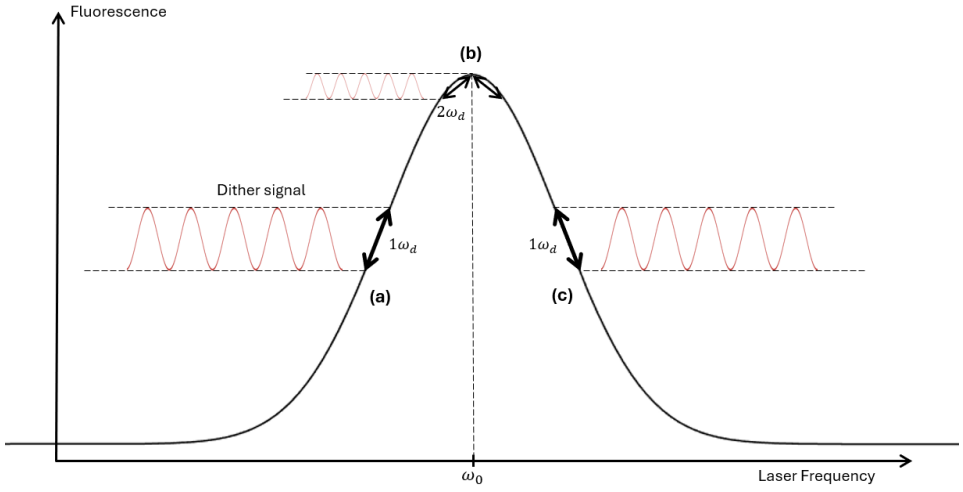

Fig. 5.8 Three possible scenarios for the laser frequency position relative to the atomic resonance during frequency modulation spectroscopy. (a),(c) Laser frequency oscillating on one side of the resonance peak; (b) Laser frequency oscillating exactly at the peak top.

If the resonance condition is not satisfied and therefore the laser is oscillating across a "side" of the peak, during one dither cycle the fluorescence increases on one half-cycle and decreases on the other, producing a signal that oscillates predominantly at ω_d.

In this case, $V_{PMT} = A\sin(\omega_d t)$ and the mixer output contains a dominant DC component (from the difference frequency term) and a smaller component at $2\omega_d$ (from the sum frequency term):

$$V_{mixer} \approx \frac{AB}{2}\left[1 - \cos(2\omega_d t)\right]. \tag{5.4}$$

After low-pass filtering, the $2\omega_d$ term is removed, leaving a DC voltage proportional to the amplitude of the fluorescence oscillation. This DC voltage acts as the error signal, showing how far the laser is detuned from the resonance peak. The same logic applies if the laser is on the other side of the peak, but then the fluorescence falls during the first half-cycle and rises during the second, producing a negative DC component after low-pass filtering. Hence, any time the laser frequency is off-resonance, the demodulated lock-in output produces a non-zero DC voltage whose sign indicates which side of the peak the laser is located and can be used for feedback control. Whenever the laser frequency is lower than the resonance frequency, the positive error signal is produced to raise the laser frequency. On the other hand, if the laser frequency is above the resonance frequency, a negative error signal is produced to lower it. Also, where the absorption line is steeper, the fluorescence changes more quickly with frequency, resulting in a larger oscillating signal and a stronger error signal after demodulation. That is why the error signal generated after demodulation has a derivative-like shape of the spectroscopic peak, as shown in Figure 5.9.

In the last scenario, if the laser frequency is oscillating exactly at the top of the peak, the laser visits the left and right sides of the line symmetrically: in both cases the fluorescence decreases and reaches the maximum, so within one dither period the signal exhibits two similar excursions (two dips), resulting in a dominant $2\omega_d$ component. In this situation $V_{PMT} = A\sin(2\omega_d t)$ and the mixer output becomes:

$$V_{mixer} = \frac{AB}{2}\left[\cos(\omega_d t) - \cos(3\omega_d t)\right], \tag{5.5}$$

leaving no DC component after low-pass filtering. Thus, when the laser frequency is exactly at resonance, the demodulated lock-in output is zero, indicating that no correction is needed.

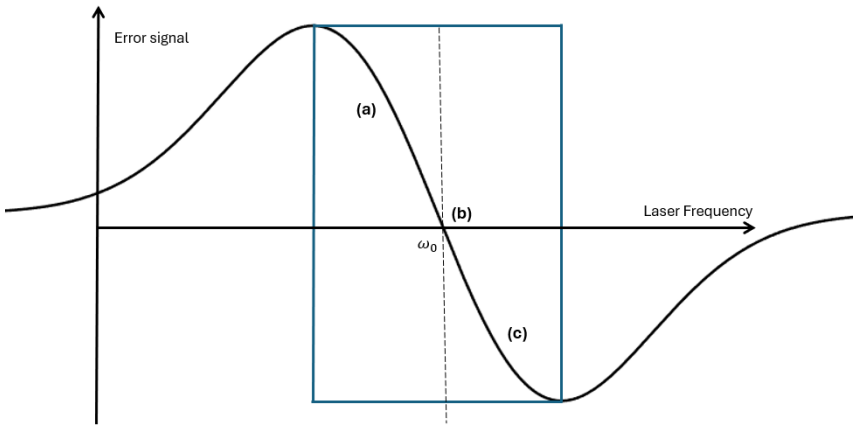

Fig. 5.9 Shape of the error signal obtained via frequency modulation spectroscopy. The laser frequency exactly on resonance produces a zero error signal (a), while detuning to the left (b) or right (c) of the peak produces a positive or negative error signal, respectively.

Finally, the error signal is fed into a PID controller, which converts the error measurement into an actuator command to lock the laser frequency to the atomic transition. This feedback loop ensures the laser is locked to the "0-error" point of the dispersive signal, corresponding precisely to the center of the two-photon resonance.

In our implementation, the laser frequency is dithered at $\approx$ 250kHz showing the error signal illustrated in Figure 5.10.

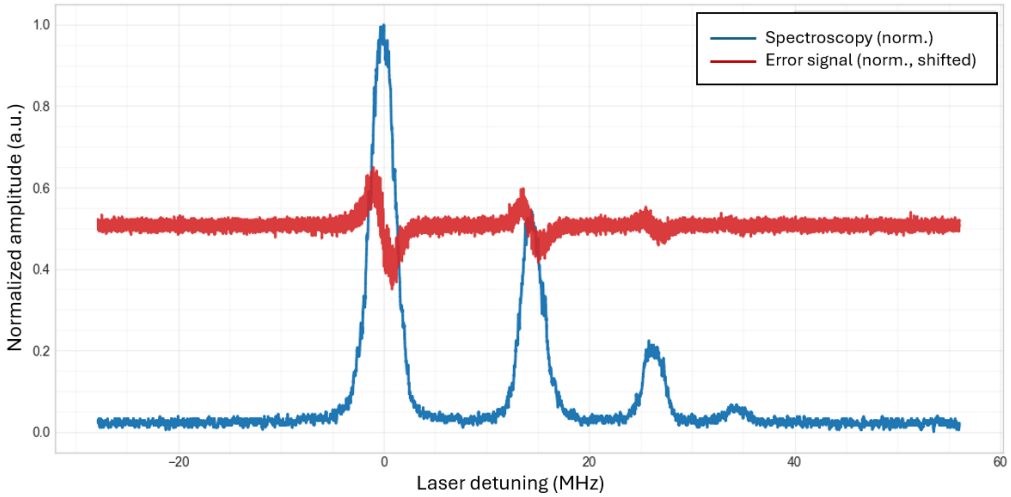

Fig. 5.10 Spectroscopic features and corresponding generated error signal for the $F_g = 2 \rightarrow F_e = 4$ two-photon transition of ^{87}Rb

5.3 Frequency Noise Characterization: Free-Running vs. Locked Laser

To quantitatively assess the performance of the laser frequency lock, we compare the frequency noise spectrum of the free-running laser against that of the locked laser. This analysis requires converting the measured lock-in output voltage into a physically meaningful frequency noise spectral density using the discriminator calibration obtained from the error signal characterization.

5.3.1 Discriminator Calibration

The first step in the analysis is to establish the relationship between voltage fluctuations at the lock-in output and corresponding laser frequency fluctuations. This calibration is obtained from the dispersive error signal measured by scanning the laser across the atomic resonance while unlocked, shown in Figure 5.10.

From a linear fit performed on the steepest part of the error signal (between the maximum and minimum), we extract the discriminator slope D, which relates voltage changes to frequency detuning:

$$D = \frac{dV}{df} \sim -3.86 \times 10^{-7} V/Hz = -0.386 V/MHz. \tag{5.6}$$

The magnitude of D quantifies the sensitivity of the frequency-to-voltage conversion, meaning that a larger $|D|$ implies a steeper error signal, which generally leads to better frequency discrimination and lower residual noise when locked.

This calibration factor allows us to translate any measured voltage fluctuation δV at the lock-in output into an equivalent laser frequency fluctuation δf via:

$$\delta f = \frac{\delta V}{|D|}. \tag{5.7}$$

5.3.2 Spectral Measurements

The frequency noise characterization was performed by recording the Fast Fourier Transform (FFT) of the error signal voltage with a phase noise analyzer, both when

the laser was free-running and when it was locked to the atomic transition. In such measurements, the horizontal axis represents the analysis frequency (Fourier frequency) and not the laser frequency detuning.

In particular, when the laser is not locked to the atomic transition, the FFT of the error signal voltage reflects the intrinsic frequency noise of the laser plus any environmental perturbations (temperature drifts, acoustic vibrations, electronic noise). On the other hand, if the laser is actively stabilized to the atomic resonance via feedback to the piezo actuator, the measured signal now reflects the residual frequency noise that the servo loop has not suppressed, plus any noise introduced by the feedback system itself.

For each dataset, multiple measurements were averaged to reduce statistical uncertainty. The averaged data consists of the FFT voltage magnitude $|V(f_F)|$ as a function of Fourier frequency f_F. This signal must be normalized by the device bandwidth resolution (multiplied by the correction factor for the FFT window used) to obtain an amplitude spectral density (ASD), that has units of $\mathrm{V}/\sqrt{\mathrm{Hz}}$:

$$S_V(f_F) = \frac{|V(f_F)|}{\sqrt{\Delta f}} \quad \left[\mathrm{V}/\sqrt{\mathrm{Hz}}\right]. \tag{5.8}$$

Finally, using the discriminator calibration from Eq. (5.6), the voltage ASD is converted to a frequency noise ASD $S_f(f_F)$, which quantifies the laser's frequency fluctuations as a function of Fourier frequency:

$$S_f(f_F) = \frac{S_V(f_F)}{|D|} \quad \left[\mathrm{Hz}/\sqrt{\mathrm{Hz}}\right]. \tag{5.9}$$

5.3.3 Results

The frequency noise amplitude spectral density as a function of Fourier frequency is reported in Figure 5.11 for four operating conditions of the laser.

The *Off-resonance* trace is acquired with the laser frequency set far from the atomic resonance. In this regime, the dispersive error signal vanishes, leading to a trace that represents the phase noise analayzer and electronics noise floor. The curve, therefore, sets the lower bound and available sensitivity for the the other

measurements in the plot and it follows an approximately monotonic slope that is not associated with any laser frequency fluctuation.

The *Unlocked* curve represents the free-running laser frequency noise instead, since it is acquired in absence of any active stabilization. As expected, according to the mechanical and thermal slow drifts that characterize a laser source, at low Fourier frequency it is clearly placed above the off-resonance noise floor. At higher frequencies, the curve is gradually approached by the slow lock curve ("Piezo Lock" trace). The slow lock introduces an active feedback stabilization that has limited correction bandwidth, effectively suppressing low Fourier frequency drifts but leaving an higher noise shoulder at the loop bandwidth edge, in which the loop gain "rolls off". This effect can be clearly observed in the range $100 - 1000Hz$, after which the slow lock is inefficient and the signal rejoins that of the unlocked laser.

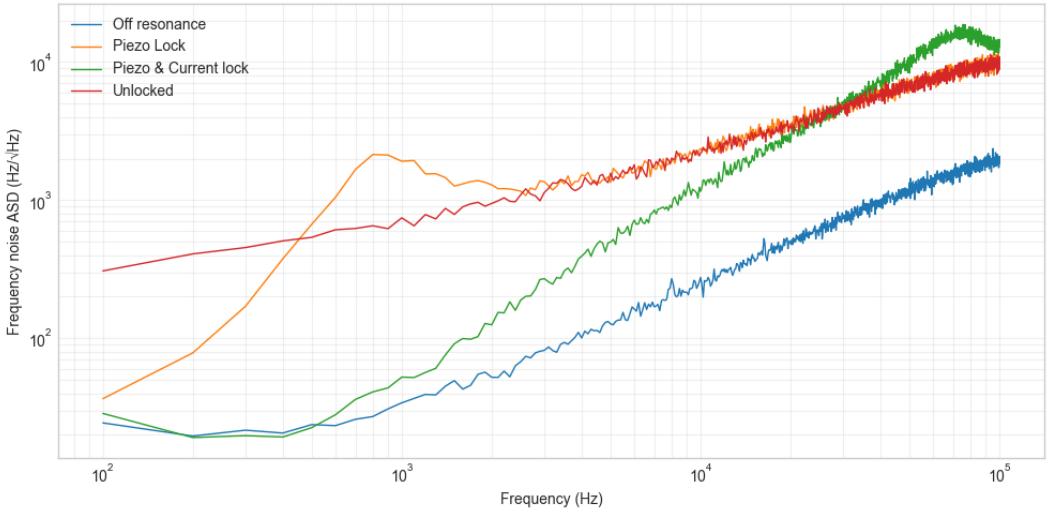

Fig. 5.11 Frequency noise ASD $S_f(f_F)$ as a function of Fourier frequency for four laser operating conditions: off-resonance (instrumental noise floor), unlocked (free-running laser), piezo-only lock (slow lock, limited bandwidth), and combined piezo-current lock (fast lock, extended bandwidth reaching the noise floor at low frequencies)

To extend the correction bandwidth, achieving oscillations suppression over a wider range of Fourier frequencies, a second feedback path that acts on the laser injection current is employed. This effect, combined with the slow lock, is shown with the *Piezo & Current Lock* trace (fast lock). At low frequencies, the fast lock directly sits on the off-resonance trace, proving that slow laser drifts are in practice entirely suppressed by the servo. This represents the primary operational requirement of an optical clock, with the laser frequency closely following the atomic resonance

and slow deviations reduced to the level of the instrumental noise floor. Finally, at higher Fourier frequencies, the fast lock introduces an excess noise originating from the current modulation itself up to the point at which the feedback loop reaches its bandwidth limit. Though this effect is clearly visible around $70-80kHz$, it would only affect clock stability at an extremely short timescale, without a meaningful impact at averaging times of interest.

It's important to note that since these acquisitions refer to the error signal of the lock-in amplifier, the frequency noise ASD directly characterizes the locking performance of the system. In other words, we are quantifying how closely the laser frequency follows the Rb two-photon transition, rather than assessing the absolute drift of the atomic resonance itself.

Nonetheless, while absolute laser stability characterization for long time intervals requires an out-of-loop measurement, which is the subject of the next chapter, the results of this section can be representative of the clock stability for short-terms, where perturbations of the atomic resonance can be negligible. Based on the results of Figure 5.11, we can express the theoretical stability limit (eq. 2.6) as a function of the detection noise amplitude spectral density N_{ASD} [81, 82]:

$$\sigma_y(\tau) = \frac{N_{ASD}}{\sqrt{2}|D|\nu_0\sqrt{\tau}} \tag{5.10}$$

where ν_0 is the absolute optical frequency of the atomic transition.

Since we already factored the discriminator calibration into the data to produce the frequency noise ASD $S_f(f_F)$ in equation (5.9), the stability estimate simplifies to:

$$\sigma_y(\tau) = \frac{S_f(f_F)}{\sqrt{2}\nu_0\sqrt{\tau}} \tag{5.11}$$

By evaluating the equation within the 10^2-10^3Hz region of the off-resonance curve, we estimate a short-term stability lower bound of $\sigma_y(\tau) \approx 3.67\times10^{-13}/\sqrt{\tau}$, a result that is in good agreement with the typical performance of two-photon rubidium standards [79].

Chapter 6

Future Developments

The frequency stability of rubidium atomic clocks depends on how stable the laser source is, which is locked to the 778nm two-photon atomic transition. In a full system, the clock laser's optical frequency is usually measured and compared to external references with an optical frequency comb. However, at the time of writing, a frequency comb was not available yet, which makes the direct optical-to-RF frequency conversion and the frequency stability evaluation not straightforward. For this reason, we are exploring an alternative approach to characterize the laser frequency stability for longer timescales by exploiting optical cavities as intermediate frequency references.

This chapter explains the theory behind using the Pound-Drever-Hall (PDH) technique to lock the laser to a high-finesse optical cavity. It also presents a model to estimate the expected frequency stability of our clock based on how the cavity operates.

6.1 Stability Measurements

In the previous chapter, frequency modulation spectroscopy with lock-in detection was used to stabilize the laser to the atomic two-photon resonance. There, a small sinusoidal dither of the laser frequency at angular frequency ω_m produced an intensity modulation of the fluorescence signal at ω_m or $2\omega_m$, and phase-sensitive demodulation yielded a dispersive error signal centered on the atomic line. The Pound-Drever-Hall technique relies on the same underlying modulation and lock-in

framework, but it's naturally described using the sideband spectral decomposition, explicitly tracking how the carrier and each sideband interact with the cavity [83].

6.1.1 Pound–Drever–Hall technique

A small phase modulation of the laser field at angular frequency ω_m with modulation index $\delta \ll 1$ (representing the maximum difference between the phase of the modulated oscillator and that of an unmodulated one) generates a carrier at ω and first-order sidebands at $\omega \pm \omega_m$ with amplitudes set by Bessel functions $J_n(\delta)$ (Figure 6.1). To first order in δ, the field after the modulation through an electro-optic modulator (EOM) can be written as

$$E_{\mathrm{FM}}(t) = E_0 \left[J_0(\delta) e^{i\omega t} + J_1(\delta) e^{i(\omega+\omega_m)t} - J_1(\delta) e^{i(\omega-\omega_m)t} \right] + \text{c.c.}, \tag{6.1}$$

i.e. a carrier plus two symmetric sidebands [84].

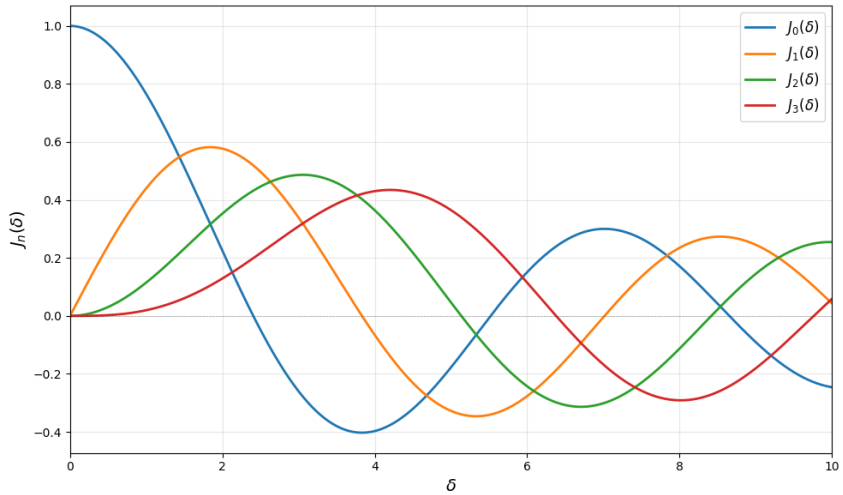

Fig. 6.1 Bessel functions of the first kind $J_n(\delta)$ of order $0 \leq n \leq 3$ versus modulation index δ.

In PDH, this modulated field is sent to an optical cavity (usually a Fabry-Pérot interferometer) serving as the frequency reference. Each frequency component is reflected with a complex reflectivity coefficient $r_{\mathrm{FP}}(\cdot)$ that depends on the specifics of the interferometer. The reflected field can be expressed as

$$E_r(t) = \frac{E_0}{2}\Big[r_{\mathrm{FP}}(\omega)J_0(\delta)e^{i\omega t} + r_{\mathrm{FP}}(\omega+\omega_m)J_1(\delta)e^{i(\omega+\omega_m)t} - r_{\mathrm{FP}}(\omega-\omega_m)J_1(\delta)e^{i(\omega-\omega_m)t}\Big] + \text{c.c.} \quad (6.2)$$

A polarization scheme (e.g. quarter-wave plate or Faraday isolator plus polarizing beam splitter) separates the reflected beam from the input and directs it onto a photodiode. The photocurrent is proportional to the reflected power,

$$i_{\mathrm{PD}}(t) \approx \eta_{\mathrm{PD}} P_r(t) \propto E_r(t)\,E_r^*(t), \quad (6.3)$$

so that beat notes between carrier and sidebands appear at the modulation frequency ω_m. Retaining only the component at ω_m (carrier–sideband interference), one can write in compact form,

$$i_{\omega_m}(t) = K\Big[A(\Delta\omega)\cos(\omega_m t) + D(\Delta\omega)\sin(\omega_m t)\Big], \quad (6.4)$$

where $\Delta\omega = \omega - \omega_0$ is the detuning from the cavity resonance ω_0, while $A(\Delta\omega)$ and $D(\Delta\omega)$ are the in-phase and quadrature components of the cavity response (analogous to absorptive and dispersive contributions in the atomic case). Finally, the constant K includes factors such as $J_0(\delta)J_1(\delta)$.

As in the atomic lock, this ω_m component is demodulated with a phase-coherent local oscillator (LO) at the same frequency,

$$v_{\mathrm{LO}}(t) = \cos(\omega_m t + \phi), \quad (6.5)$$

using a mixer (or lock-in) followed by a low-pass filter. The mixer output, after filtering out the $2\omega_m$ terms, yields a DC error signal

$$V_{\mathrm{err}}(\Delta\omega) \propto \frac{K}{2}\Big[A(\Delta\omega)\cos\phi - D(\Delta\omega)\sin\phi\Big]. \quad (6.6)$$

By adjusting the demodulation phase ϕ, one selects which quadrature is detected:

$$\phi = 0^\circ \;\Rightarrow\; V_{\text{err}}(\Delta\omega) \propto \frac{K}{2} A(\Delta\omega), \tag{6.7}$$

$$\phi = 90^\circ \;\Rightarrow\; V_{\text{err}}(\Delta\omega) \propto -\frac{K}{2} D(\Delta\omega). \tag{6.8}$$

Choosing the dispersive-like component $D(\Delta\omega)$ gives the characteristic antisymmetric PDH error signal with a steep zero crossing at cavity resonance.

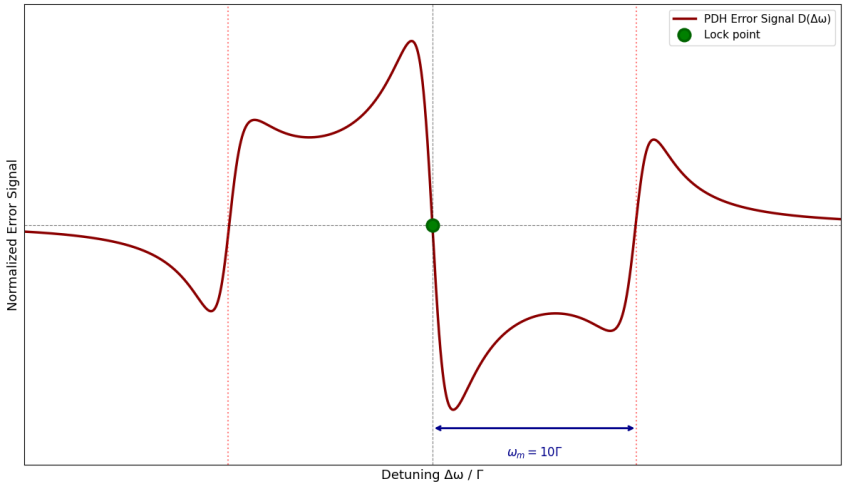

Fig. 6.2 Typical Simulated Pound–Drever–Hall error signal for $\omega_m = 10\Gamma$ (Γ being the cavity linewidth) versus the detuning from the resonance $\Delta\omega = \omega - \omega_0$.

Finally, the error signal is fed to a PID controller that stabilizes the laser frequency, completing the PDH locking loop.

6.1.2 Theoretical Cavity Stability Model

A key future objective of this work is to characterize the atomic clock frequency stability without requiring an optical frequency comb. The proposed method utilizes a stable optical resonant cavity as an intermediate-frequency reference: first, a laser is coupled to the resonant cavity using the Pound-Drever-Hall technique, and then the resonant cavity is used to study atomic transitions. The stability of the atomic reference can be be assessed by monitoring the time-varying beat note between the cavity resonance and the atomic transition frequency.

However, in order to make a significative comparison, the stability of the reference cavity has to be evaluated. This is done by a dual-cavity comparison mea-

surement, in which two independent and nominally identical optical cavities are stabilized simultaneously, and their differential frequency noise is monitored. In practice, the two cavities are not perfectly shielded from their environment, meaning they can experience different vibrations and temperature changes, which appear as a relative drift between their resonance frequencies. By measuring this drift, we directly probe the independent noise of each cavity and obtain an estimate of the short-term stability that a laser can reach when it is locked to one of them.

The dual-cavity stabilization scheme is illustrated in Figure 6.3. The setup consists of two independent branches, each implementing PDH locking to a separate optical cavity.

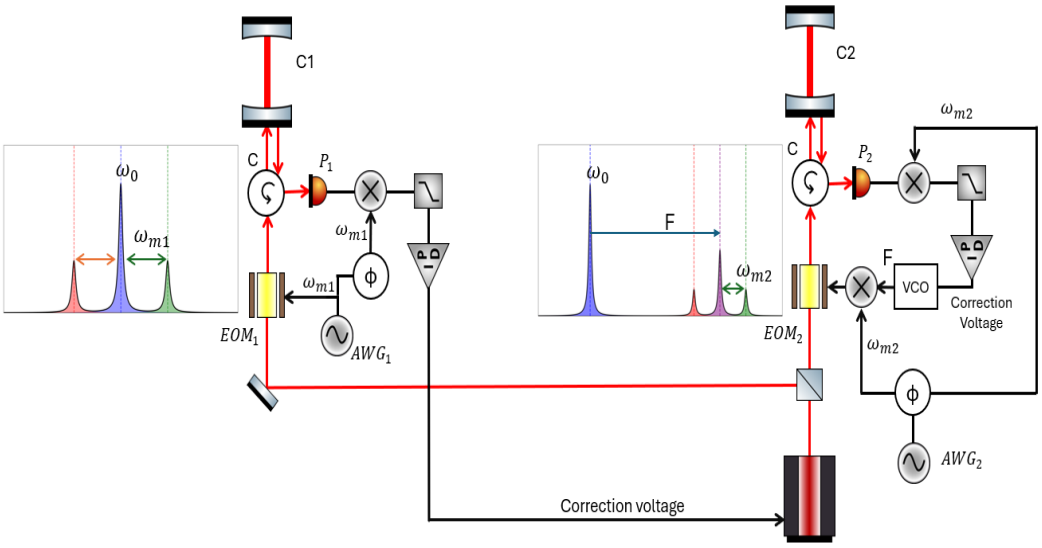

Fig. 6.3 Dual-cavity stabilization setup using the Pound-Drever-Hall technique. The laser carrier at ω_0 is locked to Cavity 1 (C1) via standard PDH. A sideband at $\omega_0 + F$ is generated and independently locked to Cavity 2 (C2). The beat frequency F between the two locks provides a measure of the differential cavity stability. C1, C2: Optical cavities; EOM: Electro-optic modulator; P1, P2: Photodiodes; VCO: Voltage-controlled oscillator; ϕ: Phase Shifter. Red lines indicate optical paths; black lines indicate electronic signals.

In the first branch, the laser carrier at frequency ω_0 is phase-modulated by the first electro-optic modulator (EOM_1) at frequency ω_{m1}, generating sidebands at $\omega_0 \pm \omega_{m1}$. This modulation is driven by an arbitrary waveform generator (AWG_1), which also provides the reference signal for lock-in demodulation. The modulated beam is sent to Cavity 1 (C1), and the reflected light is detected by a photodiode.

The photodiode signal is mixed with the reference at ω_{m1} and low-pass filtered to produce a dispersive error signal, which is fed to a PID controller that adjusts the laser frequency to lock ω_0 to a resonance of C1.

Once the laser is locked to C1, it is split off and sent to the second branch. Here, a second electro-optic modulator (EOM_2) applies a large frequency offset F (typically tens to hundreds of MHz), generating an upper sideband at $\omega_0 + F$. This sideband is then phase-modulated at a second frequency ω_{m2}, creating additional sidebands at $(\omega_0 + F) \pm \omega_{m2}$. These are used to perform PDH locking of the frequency $\omega_0 + F$ to a resonance of the second cavity (C2). The reflected light from C2 serves again to generate the dispersive error signal that is sent to a second PID controller. The PID output is fed back to the voltage-controlled oscillator (VCO) that drives the second modulator, thereby stabilizing the offset frequency F such that $\omega_0 + F$ remains locked to C2.

Because ω_0 is locked to C1 and $\omega_0 + F$ is locked to C2, the beat frequency F corresponds to the frequency difference between the two cavity resonances. Any fluctuation in F reflects the differential drift between the two cavities. By recording $F(t)$ over time and computing its Allan deviation $\sigma_y(\tau)$, we obtain a measure of the relative stability between C1 and C2.

If the two cavities are constructed identically and exhibit similar stability, the single-cavity Allan deviation can be estimated as

$$\sigma_{\text{single}}(\tau) \approx \frac{\sigma_{\text{beat}}(\tau)}{\sqrt{2}}, \tag{6.9}$$

where $\sigma_{\text{beat}}(\tau)$ is the Allan deviation of the beat frequency F. We expect the cavity C2 to provide good short-term stability, acting as a low-noise local oscillator despite being subject to slow environmental drifts. At short averaging times ($\tau \lesssim 1$ s), cavity noise (thermal, mechanical, and PDH shot noise) typically dominates, while at longer timescales ($\tau \gtrsim 10$ s), cavity frequency drifts due to thermal expansion and environmental variations become significant. This stability represents a lower bound when compared against the atomic transition stability in subsequent measurements.

6.1.3 Theoretical Clock Stability Model

Once the cavity stability is characterized, the next step is to compare the cavity-stabilized laser against the atomic two-photon transition. For this purpose the setup is reconfigured so that the left branch locks the laser directly to the atomic transition, as shown in Figures 5.2 and 5.7. Additionally, adopting a C-band laser, the second-harmonic generation cavity designed in Chapter 4 is integrated into the setup to efficiently convert the 1556 nm fundamental beam to the 778 nm second harmonic. To maximize the power available for atomic interrogation and reach the theoretical conversion efficiency presented in Section 4.1.4, an erbium-doped fiber amplifier can eventually be added to boost the input power before frequency doubling.

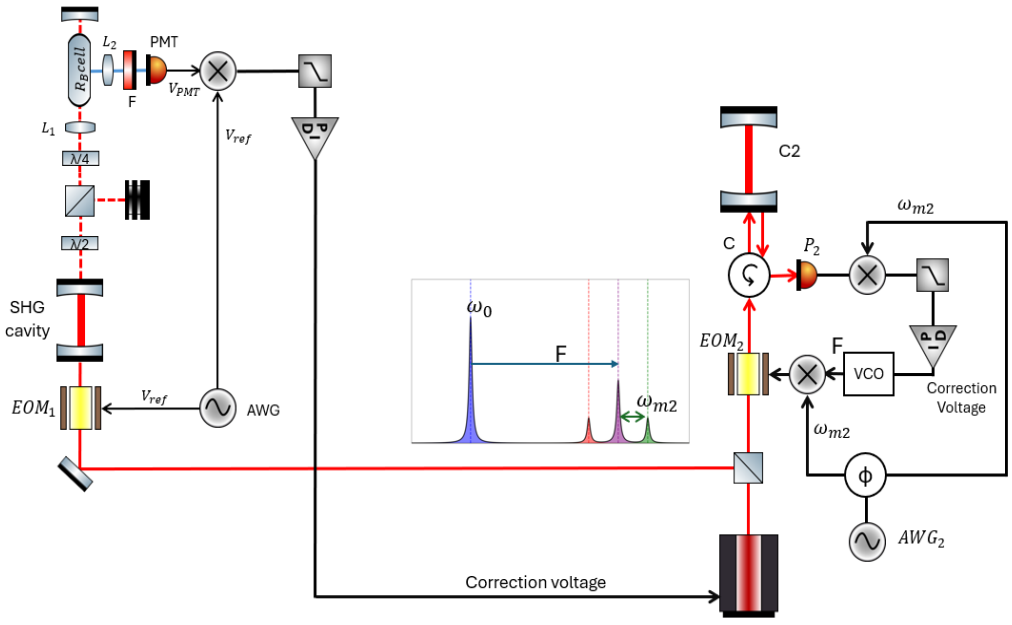

Fig. 6.4 Atomic reference-cavity comparison setup. The laser beam at 1556nm is converted into 778nm light through the frequency doubling cavity and locked to the rubidium two-photon atomic transition via frequency modulation spectroscopy (left branch). A sideband at $\omega_0 + F$ is generated and independently locked to Cavity 2 (C2) via Pound-Drever-Hall (right branch). The beat frequency F between the atomic lock and the cavity lock provides a measure of the atomic clock stability relative to the cavity reference. Solid red lines indicate 1556nm light; dashed red lines indicate 778nm light.

The right branch remains unchanged, locking the offset sideband to Cavity 2 at the beat frequency F, now reflecting the frequency difference between the atomic and the cavity resonances (Figure 6.4).

By monitoring $F(t)$ over time, we can extract the Allan deviation $\sigma_y(\tau)$ of the atomic transition relative to the cavity reference. In fact, assuming $\sigma_{\text{atom}-\text{cavity}}(\tau) > \sigma_{\text{single}}(\tau)$, i.e., the atomic instability dominates the measured beat noise at the timescales of interest, we can isolate the absolute atomic clock stability via

$$\sigma_{\text{atomic}}(\tau) = \sqrt{\sigma^2_{\text{atom-cavity}}(\tau) - \sigma^2_{\text{single}}(\tau)}. \tag{6.10}$$

If the atomic stability is better than the cavity stability at certain timescales, direct isolation of the atomic contribution from the beat measurement becomes impossible. In this regime, the measured $\sigma_{\text{single}}(\tau)$ provides only an upper bound on the atomic clock stability. However, if this upper bound is sufficiently low to meet the target performance specifications, it still serves as a valid characterization of the clock's performance.

Overall, the cavity-referenced comparison offers a comb-free approach to characterize the frequency stability of the rubidium two-photon atomic clock, improving the short term measurements of Section 5.3.3. Once the comb is available, it can be used to validate the cavity-based measurements and provide an absolute frequency reference for further improvements.

Chapter 7

Conclusions

This thesis takes the first practical steps toward building an optical clock based on the two-photon transition of ^{87}Rb. The work was divided into two main parts: the design of an optical cavity to enhance the second harmonic generation of light at 778 nm starting from a telecom laser at 1556 nm, and the construction of a two-photon spectroscopy setup to resolve and characterize the relevant atomic resonance.

For the frequency-doubling stage, we designed a compact confocal Fabry-Perot resonator. This kind of cavity allows the circulating power inside to become much higher than the input power to efficiently generate the second harmonic at 778 nm. The design was optimized to get the best possible overlap between the laser beam and the nonlinear crystal, so as to improve the conversion efficiency. Calculations, supported by numerical simulations with SNLO, show that it should be possible to obtain more than 0.5 W at 778 nm from 2 W at 1556 nm, a level well suited for the clock application. Although the ordered crystal and mirrors did not arrive in time to assemble and test the cavity during this thesis, the project is now fully defined and can be brought into operation as a direct continuation of this work.

On the spectroscopy side, we built a compact setup to observe the two-photon transition in a rubidium vapor cell. A specific choice in the layout was to place the photomultiplier tube on the side of the cell, instead of behind the retroreflecting mirror. The aim of this choice was to avoid collecting too much of the strong 778 nm light not reflected by the mirror, which would have increased the background level and made it harder to see the weak 420 nm fluorescence coming from the atoms. With this configuration, we were able to clearly see the lines of both ^{87}Rb and ^{85}Rb,

including the structure of the excited $5D_{5/2}$ state starting from the $|F_g = 2\rangle$ ground state of ^{87}Rb.

We then studied how the amplitude and linewidth of the observed peaks changed when we varied the laser power and the cell temperature, in order to find good working conditions for stabilizing the laser. The results match what is expected for a two-photon transition: the signal grows roughly with the square of the laser power, the peaks become broader at higher power, and the signal increases with temperature over the range we explored.

Using these results, we locked the laser to the $5S_{5/2} \rightarrow 5D_{5/2}$ ($|F_g = 2\rangle \rightarrow |F_e = 4\rangle$) transition of ^{87}Rb and checked the effect of the lock by looking at the amplitude spectral density of the laser noise in the locked and unlocked cases. The measurements show a clear reduction of noise at low frequencies when the lock is active, which means that the laser is indeed being kept close to the atomic resonance. These are, however, in-loop measurements, demonstrating that the servo loop operates correctly and not directly yielding the absolute frequency stability of the clock for long terms. Nonetheless, they provide an estimate of the expected short-term stability limit imposed by the electronic noise, recasting equation 2.6 in a form that includes the detection noise amplitude spectral density. The result gives a short-term stability of $\sigma_y(\tau) \approx 3.67 \cdot 10^{-13}/\sqrt{\tau}$, yilding a value that in line with standard two-photon rubidium clocks.

In the final part of the thesis, the next steps needed to complete the clock stability characterization are described. In particular, we propose to perform out-of-loop measurements using two stable reference cavities, offering a lower bound on the achievable stability with the possibility to extend measurements over larger timescales. In this scheme, the frequency-doubling cavity designed in this work will allow the use of reliable telecom-band lasers as the main light sources for the clock.

When an optical frequency comb becomes available, it will be possible to directly measure and reference the clock frequency to primary standards. At that point, the elements developed here (the design of the doubling cavity, the two-photon spectroscopy setup, and the demonstrated laser lock) will form the core of a more compact optical clock based on the two-photon transition in ^{87}Rb.

References

[1] Fritz Riehle. Towards a redefinition of the second based on optical atomic clocks. *Comptes Rendus Physique*, 16(5):506–515, 2015.

[2] Clivati C., Ambrosini R., Artz T., et al. «A VLBI experiment using a remote atomic clock via a coherent fibre link». *Scientific Reports*, 7:40992, 2017.

[3] Marra et al. «Optical Interferometry–based Array of Seafloor Environmental Sensors Using a Transoceanic Submarine Cable». *Science*, 376:874–849, 2022.

[4] Grotti J., Koller S., Vogt S., et al. «Geodesy and metrology with a transportable optical clock». *Nature Phys*, 14:437–441, 2018.

[5] Takamoto M., Ushijima I., Ohmae N., et al. «Test of general relativity by a pair of transportable optical lattice clocks». *Nature Photonics*, 14:411–415, 2020.

[6] N. D. Bhaskar, J. White, L. Mallette, T. McClelland, and J. Hardy. «A historical review of atomic frequency standards used in space systems». In *Proceedings of 1996 IEEE International Frequency Control Symposium*, pages 24–32, 1999.

[7] Prestage, John D., Weaver, and Gregory L. «Atomic Clocks and Oscillators for Deep-Space Navigation and Radio Science». *Proceedings of the IEEE*, 95(11):2235–2247, 2007.

[8] Tavella P. and Petit G. «Precise time scales and navigation systems: mutual benefits of timekeeping and positioning». *Satellite Navigation*, 1, 2020.

[9] Lombardi MA, Novick AN, Neville-Neil G, and Cooke B. «Accurate, Traceable, and Verifiable Time Synchronization for world financial markets». *Journal of research of NIST*, 121:436–463, 2016.

[10] Lecture Notes from the «Labs of Quantum Technologies» Course of Research Director Davide Calonico (INRIM, Istituto Internazionale di Ricerca Metrologica), 2024.

[11] Udem T., Reichert J., Holzwarth R., and Hänsch T. W. «Accurate measurement of large optical frequency differences with a mode-locked laser». *Opt. Lett.*, 24:881–883, 1999.

[12] Essen L. and Parry J. V. L. «An Atomic Standard of Frequency and Time Interval: A Cæsium Resonator». *Nature*, 176:280–282, 1955.

[13] Allan D. W. «Statistics of atomic frequency standards». *Proceedings of the IEEE*, 54:221–230, 1966.

[14] Bandi T. N. «A Comprehensive Overview of Atomic Clocks and their Applications». *BEMS Reports*, 9(1):1–10, 2023.

[15] Wynands R. and Weyers S. «Atomic fountain clocks». *Metrologia*, 42(3):S64–S79, 2005.

[16] Bloom B. J., Nicholson T. L., Williams J. R., Campbell S. L., Bishof M., Zhang X., Zhang W., Bromley S. L., and Ye J. «An optical lattice clock with accuracy and stability at the 10^{-18} level». *Nature*, 506:71–75, 2014.

[17] McGrew W. F., Zhang X., Fasano R. J., Schäfer J., Beloy K., Aeppli A., Robyr J.-L., Ido T., Jefferts S. R., Oates C. W., Heavner T. P., and Diddams S. A. «Atomic clock performance enabling geodesy below the centimetre level». *Nature*, 564:87–90, 2018.

[18] Dai J., Liu T., Cai Y., Chen Z., and Li Q. «Review of the development of the hydrogen maser technique and a brief introduction to its space applications». *Frontiers in Physics*, 10:966159, 2022.

[19] Cutler L. S. «Fifty years of commercial caesium clocks». *Metrologia*, 42(3):S90–S99, 2005.

[20] Schmittberger B. L. and Scherer D. R. «A Review of Contemporary Atomic Frequency Standards». *arXiv:2004.09987 [physics.atom-ph]*, 2020.

[21] Happer W., Peebles P. J. E., and Wilkinson D. T. *«Robert H. Dicke, a Biographical Memoir»*. National Academy Press, Washington, DC, USA, 1999.

[22] Chen W., Fang F., Liu K., Zheng F., Dai S., Zuo Y., and Li T. «Development of Rb fountain clock for time keeping». *Frontiers in Physics*, 10:956452, 2022.

[23] Newman Z. L., Maurice V., Fredrick C., Fortier T., Leopardi H., Hollberg L., Diddams S. A., Kitching J., and Hummon M. T. «High-performance, compact optical standard». *Optics Express*, 29(10):14176–14192, 2021.

[24] Slater J. C. *«Quantum Theory of Atomic Structure, Volume I»*. McGraw-Hill, New York, 1960.

[25] Russell H. N. and Saunders F. A. «New Regularities in the Spectra of the Alkaline Earths». *Astrophysical Journal*, 61:38–69, 1925.

[26] University of Florida — Department of Physics. «Saturated Absorption Spectroscopy Experiment (SAS)». PHY4803L — Advanced Physics Laboratory.

[27] Steck D. A. «Rubidium 87 D Line Data». 2019. Revision 1.6, steck.us/alkalidata.

[28] Steck D. A. «Rubidium 85 D Line Data». 2015. Revision 2.1, steck.us/alkalidata.

[29] Gozzelino M. and Goti I. «Atomic Spectroscopy Laboratory». Master Degree in Quantum Engineering, Politecnico di Torino, Laboratory Notes, November 2024.

[30] Wieman C. and Hänsch T. W. «Doppler-Free Laser Polarization Spectroscopy». *Physical Review Letters*, 36(20):1170–1173, 1976.

[31] Noh H.-R., Park S. E., Li L. Z., Park J.-D., and Cho C.-H. «Modulation transfer spectroscopy for ^{87}Rb atoms: theory and experiment». *Optics Express*, 19(24):23444–23452, 2011.

[32] Jacques V., Hingant B., Allafort A., Pigeard M., and Roch J.-F. «Non-linear spectroscopy of rubidium: An undergraduate experiment». *European Journal of Physics*, 30(4):735–748, 2009.

[33] Grynberg G. and Cagnac B. «Doppler-free multiphotonic spectroscopy». *Reports on Progress in Physics*, 40(7):791–841, 1977.

[34] Mark Fox. *«Quantum Optics: An Introduction»*. Oxford Master Series in Physics. Oxford University Press, Oxford, 2006.

[35] Luigi Lugiato, Franco Prati, and Massimo Brambilla. *«Nonlinear Optical Systems»*. Cambridge University Press, 2015.

[36] Robert W. Boyd. *«Nonlinear Optics»*. Academic Press (Elsevier), 4 edition, 2020.

[37] Lecture Notes from the «Quantum Photonics» Course of Professor Luigi Columbo (Politecnico di Torino), 2024.

[38] T. H. Maiman. «Stimulated Optical Radiation in Ruby». *Nature*, 187(4736):493–494, 1960.

[39] John Kerr. «A new relation between electricity and light: Dielectrified media birefringent». *The London, Edinburgh, and Dublin Philosophical Magazine and Journal of Science*, 50(331):337–348, 1875.

[40] P. A. Franken, A. E. Hill, C. W. Peters, and G. Weinreich. «Generation of Optical Harmonics». *Physical Review Letters*, 7(4):118–119, 1961.

[41] Bahaa E. A. Saleh and Malvin Carl Teich. *«Fundamentals of Photonics»*. Wiley, 3 edition, 2019.

[42] Gordon D. Boyd and David A. Kleinman. «Parametric Interaction of Focused Gaussian Light Beams». *Journal of Applied Physics*, 39(8):3597–3639, 1968.

[43] V. G. Dmitriev, G. G. Gurzadyan, and D. N. Nikogosyan. *Handbook of Nonlinear Optical Crystals*. Springer-Verlag, third revised edition edition, 1993.

[44] Crystal manufacturers. https://raicol.com/, https://www.aphalas.com, https://www.shalomeo.com/, https://eksmaoptics.com/, https://www.thorlabs.com.

[45] R. Paschotta. Spatial walk-off. https://www.rp-photonics.com. RP Photonics Encyclopedia.

[46] A. V. Smith. Snlo nonlinear optics code. Available from A. V. Smith, AS-Photonics, Albuquerque, NM.

[47] S. Kobtsev and A. Zavyalov. Efficient second-harmonic generation of cw radiation in an external optical cavity using non-linear crystal bibo. In *Proceedings of SPIE*, volume 6610, page 66100P, 2007.

[48] M. M. Fejer, G. A. Magel, D. H. Jundt, and R. L. Byer. Quasi-phase-matched second harmonic generation: Tuning and tolerances. *IEEE Journal of Quantum Electronics*, 28(11):2631–2654, 1992.

[49] Herman Vanherzeele and John D. Bierlein. Magnitude of the nonlinear-optical coefficients of ktiopo4. *Optics Letters*, 17(14):982, 1992.

[50] Laserfabriken. Ppktp. https://www.laserfabriken.com/ppktp/.

[51] X. Wen, Y. Han, and J. Wang. Comparison and characterization of efficient frequency doubling at 397.5 nm with ppktp, lbo and bibo crystals. *arXiv preprint*, 2016. arXiv:1601.07971.

[52] E. Bloise. Experimentation of entangled photon-pairs generation using an ultrafast source at gigahertz. Master's thesis, University of Padua, 2013.

[53] S. C. Kumar, M. Ebrahim-Zadeh, et al. «High-power, single-frequency, continuous-wave second-harmonic-generation of ytterbium fiber laser in PPKTP and MgO:sPPLT». *Optics Express*, 17(16):13711–13726, 2009.

[54] European Southern Observatory. «Characterization of the performance of PPKTP for the second harmonic generation of a 1319 nm Nd:YAG laser». Technical Report VLT-TRE-ESO-15731-3065, ESO, Garching, 2003. Issue 1.0, 01 August 2003.

[55] Poulain M., Latrasse C., Touahri D., and Tetue M. «Frequency stability of an optical frequency standard at 192.6THz based on a two-photon transition of rubidium atoms». *Optics Communications*, 208(4–6):307–314, 2002.

[56] Nan Ei Yu, Jung Hoon Ro, and Myoungsik Cha. «Broadband quasi-phase-matched second-harmonic generation in MgO-doped periodically poled LiNbO3 at the communications band». *Optics Letters*, 27(12):1114–1116, 2002.

[57] R. Wu, Y. Chen, J. Zhang, X. Chen, and Y. Xia. «Broadening of the second-harmonic phase-matching bandwidth in type ii periodically poled KTP». *Applied Optics*, 44(30):6443–6447, 2005.

[58] Liezun Chen, Shizhuan Lu, Youwen Wang, and Kaiming You. «Bandwidth broadening and spectrum tailoring of second-harmonic generation in transversely nonuniform quasi-phase-matching gratings with spatial spectral dispersion». *Optik*, 126(24):5149–5153, 2015.

[59] B. A. Richman, S. E. Bisson, R. Trebino, M. G. Mitchell, E. Sidick, and A. Jacobson. «Achromatic phase matching for tunable second-harmonic generation by use of a grism». *Optics Letters*, 22(16):1223–1225, 1997.

[60] Fox A. G. and Li T. «Resonant Modes in a Laser Resonator». *Bell System Technical Journal*, 40:453–488, 1961.

[61] Boyd G. D. and Gordon J. P. «Confocal Multimode Resonator for Millimeter Through Optical Wavelength Masers». *Bell System Technical Journal*, 40:489–508, 1961.

[62] Orazio Svelto. *Principles of Lasers*. Plenum Press, New York, 3 edition, 1982.

[63] Milonni P. W. and Eberly J. H. *«Laser Physics»*. John Wiley & Sons, Inc., Hoboken, New Jersey, 2008.

[64] W. P. Risk, T. R. Gosnell, and A. V. Nurmikko. *Compact Blue-Green Lasers*. Cambridge University Press, New York, 2003. Hardcover edition.

[65] Marco Pizzocaro, Davide Calonico, Pablo Cancio Pastor, Jacopo Catani, Giovanni A. Costanzo, Filippo Levi, and Luca Lorini. Efficient frequency doubling at 399 nm. *arXiv*, May 2014.

[66] E. S. Polzik and H. J. Kimble. Frequency doubling with $knbo_3$ in an external cavity. *Optics Letters*, 16(18):1400–1402, 1991.

[67] John R. Daniel, Shan-Wen Tsai, and Börge Hemmerling. Analytical approximation of the second-harmonic conversion efficiency. Preprint, University of California, Riverside, 2024.

[68] X. Zhang et al. Cavity-enhanced symmetric second-harmonic generation. *arXiv preprint arXiv:2509.20032*, 2025.

[69] O. S. Brozek, K. Schneider, and A. Hemmerich. Highly efficient cw frequency doubling of 854 nm gaalas diode laser light in an external ring cavity. *Optics Communications*, 146(1-6):141–146, 1998.

[70] Di Noia F.-S. «Realization and characterization of a 425.5 nm laser source for ^{53}Cr atoms cooling obtained via second harmonic generation». Master degree thesis, Università degli Studi di Firenze, 2016.

[71] Li D., Liu K., Zhao L., and Kang S. «a frequency shift compensation method for light shift and vapor-cell temperature shift in atomic clocks». *arXiv:2405.14281 [physics.atom-ph]*, 2024. Preprint.

[72] Callejo M., Mursa A., Vicarini R., Klinger E., Tanguy Q., Millo J., Passilly N., and Boudot R. «short-term stability of a microcell optical reference based on the Rb atom two-photon transition at 778 nm». *Journal of the Optical Society of America B*, 42:151–159, 2024.

[73] Erickson S. E. *«An Optical Atomic Clock Based on Frequency Comb Spectroscopy»*. PhD thesis, The University of Arizona, Tucson, AZ, USA, 2024.

[74] Newman Z. L., Maurice V., Drake T., Stone J. R., Briles T. C., Spencer D. T., Fredrick C., Li Q., Westly D., Ilic B. R., Shen B., Suh M.-G., Yang K. Y., Johnson C., Johnson D. M. S., Hollberg L., Vahala K. J., Srinivasan K., Diddams S. A., Kitching J., Papp S. B., and Hummon M. T. «Architecture for the photonic integration of an optical atomic clock». *Optica*, 6(6):680–685, 2019.

[75] Lemke N. D., Martin K. W., Beard R., Stuhl B. K., Metcalf A. J., and Elgin J. D. «Measurement of optical rubidium clock frequency spanning 65 days». *Sensors*, 22(5):1982, 2022. PMID: 35271129.

[76] Perrella C., Light P. S., Anstie J. D., Baynes F. N., White R. T., and Luiten A. N. «Dichroic Two-Photon Rubidium Frequency Standard». *Physical Review Applied*, 12:054063, 2019.

[77] Nguyen T. N. and Schibli T. R. «Temperature-shift-suppression scheme for two-photon two-color rubidium vapor clocks». *Physical Review A*, 106:053104, 2022.

[78] Li D., Liu K., Wang P., and Kang S. «Dual-interrogation method for suppressing light shift in Rb 778 nm two-photon transition optical frequency standard». *Optics Express*, 32:2766–2773, 2024.

[79] Obaze-Adeleke A. C., Semon B., and Bandi T. N. «A Comprehensive Review of Rubidium Two-Photon Vapor Cell Optical Clock: Long-Term Performance Limitations and Potential Improvements». *Photonics*, 12(5):513, 2025.

[80] Olson A. J., Carlson E. J., and Mayer S. K. «Two-photon spectroscopy of rubidium using a grating-feedback diode laser». *American Journal of Physics*, 74(3):218–223, 2006.

[81] Affolderbach C. and Mileti G. «A compact laser head with high-frequency stability for Rb atomic clocks and optical instrumentation». *Review of Scientific Instruments*, 76(7):073108, 2005.

[82] Mileti G. and Thomann P. In *Proceedings of the 9th European Frequency and Time Forum (EFTF)*, page 271, Besançon, France, 1995. Société Française des Microtechniques et de Chronométrie.

[83] Drever R. W. P., Hall J. L., Kowalski F. V., Hough J., Ford G. M., Munley A. J., and Ward H. «Laser phase and frequency stabilization using an optical resonator». *Applied Physics B*, 31:97–105, 1983.

[84] Riehle F. *«Frequency Standards: Principles and Applications»*. Wiley-VCH Verlag GmbH & Co. KGaA, Weinheim, 2004.